universität wien

MASTERARBEIT / MASTER'S THESIS

Titel der Masterarbeit / Title of the Master's Thesis

„Tunable Raman spectroscopy of single-chirality (n,m) carbon nanotubes“

verfasst von / submitted by

Eva Gabriela Röck BSc

angestrebter akademischer Grad / in partial fulfilment of the requirements for the degree of

Master of Science (MSc)

Wien, 2020 / Vienna, 2020

Studienkennzahl lt. Studienblatt / degree programme code as it appears on the student record sheet:	A 066876
Studienrichtung lt. Studienblatt / degree programme as it appears on the student record sheet:	Master Physics
Betreut von / Supervisor:	Univ.-Prof. Mag. Dr. Thomas Pichler

Abstract

Aim of this thesis is to contribute to the understanding of the electronic properties of structure-enriched specimen of single walled carbon nanotubes (SWCNT) by Raman scattering methods. The experimental investigation of ten single-chirality (n,m) probes of SWCNT via tunable Raman spectroscopy and Fourier transform (FT) Raman is concluded. Firstly, the thesis describes the relevant background regarding the materials, as well as the method. This paths the way for the interpretation of modes corresponding to SWCNT properties. Samples of single-chirality SWCNT with the characteristic indices (6,5), (8,3), (8,6), (9,1), (9,2), (9,4), (9,5), (10,0), (10,3) and (M)-(6,5) were fabricated using gel-chromatography by the group of *Kataura et al.* The samples in aqueous solution are sealed in $2\mu l$ capillaries and also dropcasted on Si-wavers for the measurements. Seven laser wavelengths in the range from 458nm to 647nm are used to excite, approaching the E_{22} transition energy. The results are complemented by FT Raman and a further Raman system that operates in the infrared at 785nm. The chosen analysis strategy, compares the experimental resonance with the expected transition energies reported in literature. The dominant radial breathing mode (RBM) is assigned to the enriched tube type. The diameters obtained from the experimental RBM frequency deviates from the reported values by 4% on average. A comparison of the RBM position for both preparation methods is introduced, to exclude a frequency shift from environmental effects. The dropcasted samples are found a convenient alternative to the liquids. They provide easier handling and focusing, a known reference from the Si background and higher total signal. Furthermore, the enrichment in the single-chirality sorted specimen is discussed. Therefore, the relative RBM intensity related to a enriched (n,m) is compared between the ten probes. Also the RBM composition of the ten chiralities is presented for each specimen. Highlighted are the spectral properties of the (M)-(6,5) nanotube as an optical isomer of the (6,5). The degree of freedom for handedness and stereochemistry cannot be elucidated using Raman, as the electronic structure for these enantiomers is identical. Therefore, the resulting spectra are expected to be congruent. Raman excitation profiles (REP) for this pair reveal that only intensity differences occur, which most probably is based on concentration. The REP are produced in steps of 2nm using an advanced dye laser system. The excitation window from 564nm to 578nm is limited by the emission spectrum of the radiant dye.

Zusammenfassung

In der vorliegenden Masterarbeit wird die monochirale (n,m) Anreicherung von einwandigen Kohlenstoff Nanoröhren (SWCNT, engl. single walled carbon nanotubes) unter Verwendung von Raman Streumethoden betrachtet. Im ersten theoretischen Teil werden nicht nur die Grundlagen zu Material und Methode erklärt, sondern auch auf die Interpretation der experimentellen Resultate vorbereitet. Wichtig dabei ist das Verständnis der Zusammenhänge zwischen dem Aufbau von SWCNT und ihrer elektronischen Bandstruktur. Der experimentelle Teil der Arbeit geht auf die angewandte Probenherstellung und den Messaufbau ein. Proben von sortierter Chiralität mit den charakteristischen Indizes (6,5), (8,3), (8,6), (9,1), (9,2), (9,4), (9, 5), (10,0), (10,3) und (M) - (6,5) in wässriger Lösung wurden auf Si-Substrate eingetropft. Eine zweite Serie an Lösung wurde in Kapillaren versiegelt und im flüssigen Zustand untersucht. Es wird ein Vergleich der radialen Atmungsmode (RBM, engl. radial breathing mode) Position für beide Präparationsmethoden vorgestellt, um eine Frequenzverschiebung durch Einflüsse aus der Umgebung oder durch Clusterbildung auszuschließen. Das verwendete Raman Spektrometer bietet sieben anregende Laserwellenlängen im Bereich von 458nm bis 647nm. Darüber hinaus werden Fourier Transformation (FT) Raman Spektren und eine Messreihe im Infrarot-Bereich ergänzt. Die Analyse vergleicht die experimentell bestimmte Resonanz mit den in der Literatur angegebenen erwarteten E_{22} Übergangsenergien und diskutiert die Qualität der Anreicherung. Dafür werden die resonanten Atmungsmoden (RBM, engl. radial breathing mode) Intensitäten, die einem Röhrenkandidaten zugeordnet sind, für die zehn Proben gegenüber gestellt. Besonders interessant sind dabei die spektralen Eigenschaften des (M)-(6,5) Typs als optisches Isomer (Spiegelbild) von (6,5). Raman Streuung kann den Freiheitsgrad für Händigkeit und Stereochemie nicht auseinanderhalten, da die elektronische Bandstruktur für diese Enantiomere identisch ist. Die resultierenden Spektren sollten daher deckungsgleich sein. Für dieses Paar mit linker (Vorsilbe M- für Minus) und rechter Helizität wird ein Raman Resonanzprofil in der Nähe des E_{22} Übergangs mit einem Farbstofflasersystem in Schritten von 2nm erstellt. Es treten nur Intensitätsunterschiede auf, was höchstwahrscheinlich auf unterschiedlichen Konzentrationen beruht. Ziel dieser Arbeit ist es, einen Beitrag zum Verständnis der elektronischen Eigenschaften von strukturangereicherten Proben aus SWCNT mittels Raman Spektroskopie zu leisten.

List of Figures

List of Tables

Contents

Abbreviations

Table 1: Alphabetical list of all abbreviations in the thesis.

Abbreviation	Explanation
BZ	Brillouin Zone
CNT	Carbon nanotubes
CNT-FET	Carbon nanotubes field-effect transistor
DFT	Density Functional Theory
DOS	Density of states
DNA	Deoxyribonucleic acid
FT	Fourier Transform
G^+; G^-mode	In-plane vibrational mode along tube axis- along circumference, respectively
IUPAC	International Union of Pure and Applied Chemistry
D mode	Intervalley scattering, LO or TO mode with q=2k
LO, TO	Longitudinal optical, transverse optical
MOSFET	Metal oxide semiconductor field-effect transistor
M-(n,m)	Minus, negative helical nanotube
MO	Molecular orbital
2D mode	Overtone of D mode
P-(n,m)	Plus, positive helical nanotube (prefix dropped in general)
RBM	Radial Breathing Mode
REP	Resonance excitation profile
RRS	Resonance Raman Spectroscopy
SWCNT	Single walled carbon nanotubes
TB	Tight Binding
TEM	Transmission Electron Microscope
vHS	van Hove Singularity
QHO	Quantum harmonic oscillator

1 Introduction

The semiconductor market is rapidly increasing with electronic devices which we perceive indispensable right now (smartphones, notebooks, light emitting diodes) and in future (Internet of Things). Current Si based components reach their limits regarding fabrication prize, size, weight, capacity and chemical tunability [1,2]. A modern generation of components made from carbon nanotubes (CNT), which can be produced from such a simple raw material like methane gas, sounds promising [3].

Since the 1990s numerous events happened, which path the way for the compilation of this thesis in 2020. Starting with the discovery of carbon nanotubes, which is accredited to Sumio Iijima in 1991 [4]. The carbon nanotubes were referred to as *helical microtubules of graphitic carbon* when they were a by-product deposited on the cathode during the arc-evaporation synthesis of fullerenes C_{60}. Followed by the theoretical predictions of the striking electronic behaviour of single-walled carbon nanotubes (SWCNT) and methods to produce them in 1992 and 1993 [5]. The exhibited extraordinary physical properties, valuable in a wide range of technologies such as electronics, optics and nanotechnology, are reported subsequently. They are stronger than steel, as ductile as plastic composites, promise ultra-compact devices and exhibit better electrical and thermal conductivity than almost any other material ever discovered [6].

It can be stated that carbon nanotubes is a material of comparatives. Therefore, research and innovation authorities are promoting their implementation in everyday devices. To mention CNT transparent conductive films as one of many examples, which are based on the exceptional charge transport in comparison to common doped metal oxides [7]. This material could advance our personal electronic devices as well as solar cells or radiation sources [8, 9]. Competing conventional metal oxide semiconductor field-effect transistors (MOSFET), field-effect transistors composed of CNT (CNT-FET) were already presented in the year 1998 [10]. Eightteen years later, ballistic charge transport close to the quantum limit of conductance $2G_0 = 4e^2/h$ was achieved in CNT-FET, exceeding those of the frequently used materials Si and GaAs [2].

Their properties can be in principle translated into macroscopic-scaled materials composed of SWCNT, but it is difficult to predict for a mixture of CNT types [11]. Many applications rely on the microscopic structure, for example semiconducting tubes with predefined band gaps for transistors. The performance of such a macro-scale device would suffer from a distribution of CNT types. In many cases we need solely the defined SWCNT type with its forecasted properties for an application, but the selective fabrication is still challenging [12]. Therefore, post-synthesis sorting methods play an important role in the processing of SWCNT. Following development of nanocomposites is caught on questions about interfacial engineering, dispersion, and effective load transfer as well [3]. So, after two decades of intensive research, the practical impact of carbon nanotube composites is still vague [3]. Specific fundamental research is

necessary dedicated to understand their behaviour, particularly in the chirality separated form in order to overcome the processing challenges. Raman spectroscopy is commonly utilized for the investigation of SWCNT in solution and solid state [13]. It provides sensitive, precise and non-destructive information on the population of nanotubes that have inter-band transitions close to the operating laser energy.

At this point the present thesis takes action. The aim of this Master thesis is to evaluate the stage of carbon nanotube processing, i.e. separation, as well as experimentally contribute to the understanding of their properties. This goal is approached by a review of literature and also by examining specimens using Raman spectroscopy methods. The present structure-enriched samples, fabricated by one of the groups with highest reputation [14], are investigated in liquid and dropcasted form. This leads to the definition of two research questions.

1. Research Question: Do we observe environmental interactions or deviations in the Raman spectra of solid versus solution SWCNT?
2. Research Question: What is the stage of SWCNT post-synthesis selection by multi column gel-chromatography recently?

The progressive method for the Master thesis can be represented by three milestones or chapters 2,3,4 respectively.

Chapter 2: The investigation begins by an overview of the background essential to understand the concepts of the theoretical - and experimental part. The literature research provides a fundamental starting point and is transformed into a qualitative chapter. Firstly, material related fundamentals and method related fundamentals are introduced. In particular, the electronic properties of SWCNT and their origin is in the focus of chapter 2.1. It is building a bridge from the relation of SWCNT to the 2D allotrope graphene, over the circumferential quantum confinement, to van Hove peaks and Kataura plots. Herein, also the stage of processing is reported and the multi-column gel-chromatography explained in greater detail, because it is the method used for separation of the investigated sample structures. Furthermore, reported Kataura plots and energy transitions for the ten investigated SWCNT types are compared with the available options in the laboratory. For the Raman scattering the classical and the quantum mechanical description are introduced. Highlighted are the vibrational modes associated with the CNT structure. This paths the way for the systematic approach of the Raman measurements. The thesis should be self-consistent within a reasonable length and therefore it is supported by references to literature.

Chapter 3: Next, a transition to the experimental part takes place, which is again sub-divided in one part for the sample description and one for the optical equipment. The sample preparation should not consume a large amount

of solution, have a defined reference and an appropriate handling. Dropcasted samples on Si are found a convenient option and solution in thin capillaries sealed with heat are added subsequently. The advantages and disadvantages of both are considered for each experimental system. The experimental setup for the available Raman system, the FT Raman and the resonance excitation profiles (REPs) is presented in a descriptive manner.

Chapter 4: Following after those assessing points, the Raman spectra are recorded and the main features RBM, G mode and 2D mode analysed in detail. The characteristic wavenumber ranges are illustrated gathered for all excitations of the sample. The Raman spectra for the dried droplets and the sealed solution are concluded first and are seen as the main achievement. Possible differences from the dropcasted sample environment are examined by the RBM peak position. There are no significant shifts observed in comparison to the liquid form, while the signal to noise ratio is higher. Next, the spectra are analysed regarding the RBM composition in each enriched specimen. The occurrence of multiple resonant RBM peaks in distance from the reported transitions energies already indicate the presence of more chiralities. The relative mode intensities are introduced in a stacked bar diagram, adding up to 1 for the total resonant modes in the sample. Moreover, to estimate the enrichment a further bar diagram illustrates relative contribution of RBM intensity arising in the various mixtures. The composition between the sub-set of the ten enriched specimen is shown in a bar diagram, normalized such that the sum of all modes at the same frequency yields 1. The FT Raman is conducted subsequently, but thre is no strongly resonant RBM observed in any of the samples. Lastly, from these results it is concluded that the Raman excitation profiles of the RBM and G mode phonon for the species (6,5) and M-(6,5) are especially interesting. The presented findings conclude the last step for an interesting discussion of the research questions.

2 Theoretical Background

2.1 Material related Fundamentals

This chapter starts with the description of the structure of SWCNT, as it determines the electronic properties and give the motivation of post-synthesis selection methods. The background is of importance to understand the response in Raman scattering systems and thus the following chapters. It mainly follows the reference [15] unless otherwise stated.

2.1.1 Structural properties of SWCNT

Single walled carbon nanotubes (SWCNT) are one of the multiple allotropes of carbon. They are imagined as a seamless hollow tube comprised of a single layer of graphene. Due to the definite length of C–C bonds there are restrictions on the cylindrical arrangement. The diameter and chirality characterize the unique geometry of these quasi one-dimensional structures. The chirality vector is defined as a linear-combination of the base vectors of the hexagonal lattice.

$$\vec{C_h} = (n, m) = n * \vec{a_1} + m * \vec{a_2}, \tag{1}$$

with the base vectors $\vec{a_1}$,$\vec{a_2}$ as stepsize and the indices (n,m) as the number of steps. The geometrical construction is shown in figure 1, where the honeycomb lattice is oriented such that the zigzag structure lies horizontally. Its magnitude is equal to the circumference of the nanotube. It connects two crystallographic equivalent locations on the honeycomb pattern of sp^2-bonded carbon atoms. The periodicity along this roll-up vector results in a tube with helical and translational symmetry along its axis. Considering again the honeycomb crystal lattice of a graphene sheet, the translational vector $\vec{T}$ is the shortest vector connecting two identical sites on the lattice while parallel to the tubular axis. It defines the unit cell of a nanotube. The vector product between the chirality vector and the translational vector $\vec{C_h} \times \vec{T}$ gives the area of the unit cell of a carbon nanotube. The diameter d of a (n,m) type carbon nanotube is determined by equation 2.

$$d = \frac{C_h}{\pi} = \frac{a_{C-C}}{\pi}\sqrt{3(m^2 + mn + n^2)} \tag{2}$$

Herein, the nearest neighbour center to center distance for graphite-like materials is $a_{C-C} = 1.42\mathring{A}$. The diameter is in the dimension of nanometers, the tube with the smallest diameter of $0.3nm$ is from (2,2) type and was characterized by a combination of Raman spectroscopy, Transmission Electron Microscopy (TEM) and theoretical density functional theory (DFT) calculations [16]. In the year 2013 a procedure of optimal processing parameters was proposed to synthesize nanotubes with half a metre (550mm) length [17].

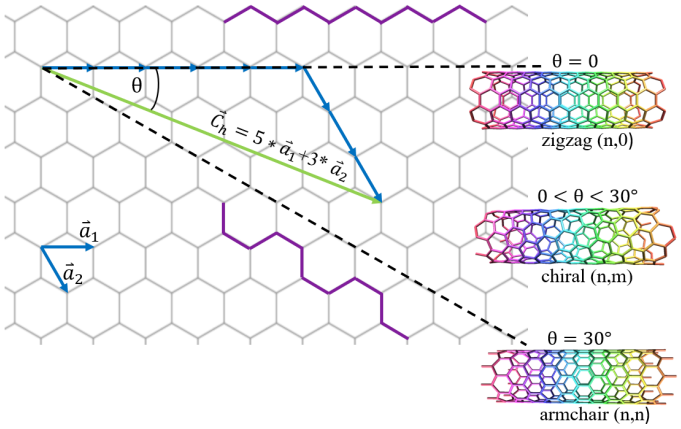

Figure 1: Representation of the hexagonal lattice base vectors a_1 and a_2 and the chiral angle θ. On the right part is the definition of the achiral cases zigzag (n,0), armchair (n,n) and chiral (n,m) nanotubes. The figure is based on reference [18] with modifications.

The chiral angle is defined as the angle spanned between the first base vector and the roll-up vector. The first base vector $\vec{a_1}$ in the illustration is oriented horizontally. With trigonometrical considerations and plugging in the definitions of the two relevant vectors (see table 2.1.1) we get the formula for the chiral angle.

$$tan\theta = \frac{\sqrt{3}m}{2n+m} \tag{3}$$

The zigzag (n,0) structure and the armchair (n,n) structure are achiral cases, with $\theta = 0$ and $\theta = 30°$ respectively. Chiral tubes with $0 < |\theta| < 30°$ can not be superimposed with their mirror image, which leads to a degree of freedom for the handedness. The terminology of tubes with the same helicity, but different handedness is often (n,m) versus (m,n) [19]. Whereas, according to the IUPAC nomenclature the prefix M (minus) is proposed for left-handed nanotubes and P (plus) for right-handed ones, e.g. (M)-(8,6)-SWCNT [20]. The common convention is usually using right-handed systems and the prefix P is frequently dropped.

The unit vectors of the honeycomb lattice define the reciprocal lattice unit vectors $\vec{b_1}$ and $\vec{b_2}$ by $\vec{a_i}\vec{b_j} = 2\pi\delta_{ij}$, with the Kronecker delta 1 for equal indices and 0 for others. The reciprocal unit vectors are rotated by 30° with respect to the real unit vectors. As the unit cell of the nanotube in real space is characterized by the chirality vector C_h and the translational vector T, the reciprocal space vectors $\vec{k_\perp}$ and $\vec{k_\parallel}$ can be deduced from the definition $\vec{C_h}\cdot\vec{K_\parallel} = \vec{T}\cdot\vec{k_\perp} = 0$. In other words, the reciprocal space vector $\vec{k_\perp}$ is orthogonal to the translational vector and the vector $\vec{k_\parallel}$ is orthogonal to the chiral vector. Their magnitude stems from $\vec{C_h}\cdot\vec{k_\perp} = \vec{T}\cdot\vec{k_\parallel} = 2\pi$ and yields $|\vec{k_\perp}| = 2/d$ and $|\vec{k_\parallel}| = 2\pi/|\vec{T}|$. The

reciprocal space vectors become important in the prediction of the electronic properties. Finally, it is necessary to define the Brillouin zone (BZ), which importance emerge in the electronic structure description. The BZ is a unit cell in reciprocal space constructed by symmetry considerations, such that all points within its bounds are closer to a central reciprocal lattice point than to any further reciprocal lattice point. It provides a wavevector representation within $-\pi/a \leq k \leq \pi/a$ appropriate to the specific real lattice. The number of possible wavevectors inside the BZ is equal the number of unit cells in the real lattice. The description of the electronic structure is complete within the first BZ, outside follow identical repetitions. The high symmetry points in the center Γ, the corners K and the center of the hexagon edge M span the irreducible zone. The two-dimensional Brillouin zone of SWCNT is shown in figure 2. The table 2.1.1 provides a list of the introduced parameters and their mathematical formulas or values.

Table 2: Parameters and their mathematical formulation and description relevant for the structural properties of SWCNT. The table is based on Table2.1 from reference [15]

Parameter	Formula / Value	Explanation
a_{C-C}	$1.42\mathring{A}$	Nearest neighbour center to center distance in graphite-like materials
a	$\sqrt{3}a_{C-C}$	Graphene lattice constant
$\vec{a_1}; \vec{a_2}$	$a(\frac{\sqrt{3}}{2}, \frac{1}{2})$; $a(\frac{\sqrt{3}}{2}, -\frac{1}{2})$	Graphene lattice unit vectors
$\vec{b_1}; \vec{b_2}$	$\frac{2\pi}{a}(\frac{1}{\sqrt{3}}, 1)$; $\frac{2\pi}{a}(\frac{1}{\sqrt{3}}, -1)$	Graphene reciprocal lattice unit vectors
$\vec{C_h}$	$n * \vec{a_1} + m * \vec{a_2} = (n, m)$	Nanotube chirality vector
d	$\frac{C_h}{\pi} = \frac{a\sqrt{m^2+mn+n^2}}{\pi}$	Nanotube diameter
θ	$tan\theta = \frac{\sqrt{3}m}{2n+m}$	Nanotube chiral angle
$\vec{T}$	$t_1 * \vec{a_1} + t_2 * \vec{a_2} = (t_1, t_2)$	Translational vector
$\vec{k_\perp}; \vec{k_\parallel}$	$\vec{C_h} \cdot \vec{k_\parallel} = \vec{T} \cdot \vec{k_\perp} = 0$ $\lvert\vec{k_\parallel}\rvert = \frac{2\pi}{\lvert\vec{T}\rvert}$ $\lvert\vec{k_\perp}\rvert = \frac{2}{d}$	Nanotube reciprocal lattice vectors
Γ; K; M	$\Gamma = (0, 0)$; $K = \frac{\pi}{a}(0, \frac{4}{3})$; $M = \frac{\pi}{a}(\frac{1}{\sqrt{3}}, -1)$	High symmetry points in graphene BZ

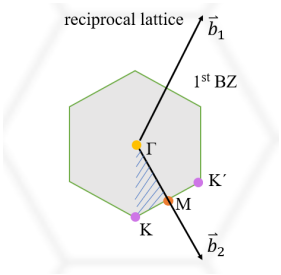

Figure 2: Schematic illustration of the first Brillouin Zone (BZ) of graphene with high symmetry points Γ, K and M. The irreducible zone is the dashed area and the reciprocal lattice vectors $\vec{b_1}$ and $\vec{b_2}$. The figure is based on reference [21] with modifications.

2.1.2 Electronic structure deduced from graphene

The optical and electronic properties strongly depend on the underlying geometry. The band structure of SWCNT therefore, can be deduced from the one of graphene using the zone-folding scheme. Thereon, additionally taking into account the one-dimensional quantum confinement along the circumference. This chapter will explain the band structure of graphene and the confinement relation, referred to as sub-bands or cutting lines for SWCNT.

In the low dimensional carbon materials, an s-orbital and two p-orbitals from the valence shell combine to form three energy equivalent sp^2 hybridized orbitals. They distinguish by spatial orientation of 120°, which determines the atomic arrangement by planar σ bonds sp^2 in a honeycomb lattice. Due to the hybridization, every fourth electron in each carbon atom is delocalized, meaning the remaining p-orbitals perpendicular to the atomic layer interact with each other and form π bonding or π^* antibonding orbitals [21]. Hence, every fourth electron can freely move through the structure. The bandstructure of graphene has characteristic cone shaped features at the Dirac points. The Fermi level is in the plane of the touching points, below is the valence band and above the conduction band. Graphene is a Zero bandgap semiconductor, whereas SWCNT differ based on where the quantization condition meets the cones. The band structure of SWCNT is represented by sub-bands on the energy surface of graphene, which is depicted in figure 3 from reference [15].

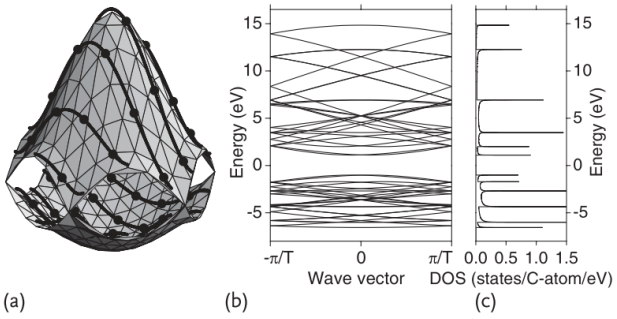

Figure 3: (a) Depiction of the valence- and conduction energy surface of graphene in the first BZ calculated by the nearest neighbour TB model. Solid curves represent the sub-bands for (4,2) SWCNT. (b) From zone-folding of the former one gets the band diagram in the reduced representation. (c) Corresponding vHSs in the DOS [15].

The σ and σ^* bands separate multiple eV at the zone center Gamma Γ point. Therefore, only the π and π^* bands are taken into account, embodying the valence and conduction band respectively. They are described by a Hamiltonian $\hat{H}$ in the Tight-Binding Approximation with base vectors parallel to either the roll-up vector C_h or the translational vector T. In greater detail, the Tight Binding Approximation is compared to *ab initio* calculations and a set of interaction parameters is introduced to depict the band structure over the whole BZ [22]. The analytical solution of the Schrödinger equation ($\hat{H}\Psi = E\Psi$) determines the energy dispersion relation, i.e. the depiction of energy bands in dependence of the wavevector components $E(k_\parallel; k_\perp)$ parallel and perpendicular to the tube axis (equation 4). Herein, the electronic wavefunction can be described by Bloch waves modulated by periodicity of the tube $\Psi(r+C_h) = e^{i\vec{k}\vec{C_h}}\Psi(r) = \Psi(r)$. E is the dispersion of an electron in a nanotube with periodicity in k, neglecting the in-plane dispersion for properties close to Fermi energy. The energy dispersion spreads in two parts $\pm$ for the lower π bonding and the upper π^* antibonding energy band [21]. The π and π^* bands are responsible for the typical cone-shape dispersion relation at the vertices of the first Brillouin Zone (BZ), see figure 4 inset. It is commonly shown for the first Brillouin zone (BZ) and the proposed interaction parameter for optical transitions, which are smaller than four electronvolts, is $\gamma_0 = -2.79eV$ [22]. The lattice constant is defined as $a = \sqrt{3}a_{C-C}$.

$$E^{\pm}(k_\parallel; k_\perp) = \pm\gamma_0\sqrt{1 + 4cos\left(\frac{\sqrt{3}k_x la}{2}\right)cos\left(\frac{k_y a}{2}\right) + 4cos^2\left(\frac{k_y a}{2}\right)} \qquad (4)$$

The states in vicinity to the Fermi energy determine the electrical conductance. The Fermi surface is localized by the first BZ vertices, which are at

$\vec{K} = (\vec{b_1} - \vec{b_2})/3 = (0, 4\pi/3a)$ and referred to as Dirac points or K points. It is to mention, that the dispersion relation $E(k)$ is linear at the K point [15]. Transitions between these cone tips are referred to as first order.

2.1.3 The quantum confinement in nanotubes

It is shown that transistors made from a single-walled carbon nanotube quantum wire, exhibit conductance close to the quantum limit of $2G_0 = 4e^2/h$ [2]. In a quantum wire or nanowire the electrons experience quantization in their transverse energy. In a nanotube the electrons are in one-dimensional confinement and the transport is ballistic, i.e. without internal scattering. The quantum effect for electron transport is more relevant for wires with smaller diameters, typically given in nanometers. The cyclic boundary conditions for carbon nanotubes give discrete allowed k-values, i.e. the perpendicular wavevector component $k_\perp$ fills the circumference seamlessly when

$$\vec{k} * \vec{C_h} = 2\pi j \tag{5}$$

with j is an integer and the length of the chirality vector is π times the diameter. This quantization leads to one-dimensional sub-bands for electrons in axis direction $k_\parallel$, where these coincide the 3D cone-shaped band structure sets the properties. The band-folding scheme describes it as a superposition of the present eigenvalues of graphene, folded in the direction of the ΓK line [21]. When the allowed k-states coincide with the Fermi surface, where the occupied and unoccupied bands degenerate by symmetry, the SWCNT is metallic. Whereas semiconducting behaviour occurs if the Dirac point wave vector $\vec{K}$ is forbidden.
The density of states (DOS) of the one-dimensional SWCNT with sharp maxima at every sub-band edge divers from that of the materials higher dimensionality. The typical DOS of a three dimensional system has a $\sqrt{E}$ dependency, for a two dimensional system it is displayed in a step function, whereas for a one dimensional system it has a $1/\sqrt{E}$ dependency. These thresholds with very high values of the DOS are the characteristic van Hove singularities (vHSs) and they are followed by a decaying tail until the next sharp rise. For energies below the first vHS the DOS is Zero for semiconducting SWCNT [15]. The corresponding band gap for semiconductors E_g is depending on the wave vector distance to the K point $\vec{k} = \vec{K} + \delta\vec{k} = (\delta k_x, 4\pi/3a + \delta k_y)$, i.e. the tight binding overlap in terms of energy or interaction parameter γ_0. It displays an inverse proportionality to the nanotube diameter d as depicted in equation 6.

$$E_g = \frac{\gamma_0 a_{C-C}}{d} \tag{6}$$

The vertex is located at one-third of the distance separating two sub-bands $k = \Delta k/3 = 2/3d$, what leads to the prominent $n - m = 3 * j$ rule for metallic or semiconducting tubes [23]. Figure 4 shows the relation between the hexagonal graphene Brillouin Zone and the electronic classification of SWCNT in a schematic manner.

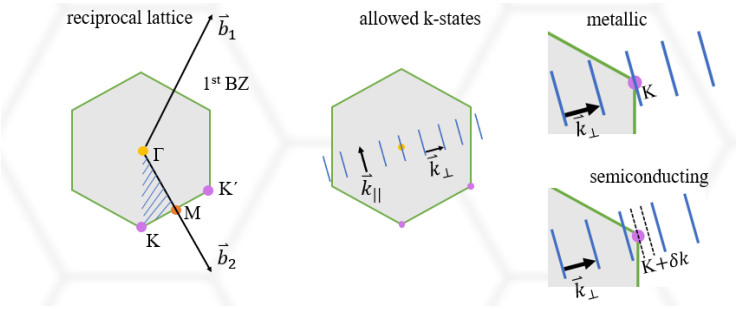

Figure 4: Schematic illustration connecting the electronic classification with geometry in reciprocal space. On the left the first Brillouin Zone (BZ) of graphene with high symmetry points Γ, K and M. Shown in the center is a depiction of the discrete k-states separated by Δk. On the right the classification as metallic if the wave-vector matches the K point. The band structure with a zoom to the Dirac point shown as an inset. The figure is based on reference [21] with modifications.

To sum up, the SWCNT are classified as metallic or semiconducting based on the diameter or indices (n,m). For an arbitrary (n, m) vector, the number $n-m$ defines the number of parallel cutting lines that cross the line connecting two BZ centers. Tubes show metallic or quasi-metallic behavior if $n-m$ is evenly divisible by 3, while significant band gaps up to half an eV and semiconducting behavior occurs if not [21]. Therefore, two out of three SWCNT with random chirality indices are semiconductors with the band gap directly depending on the present diameter. Necessarily, to mention that exceptions to this rule exist in small-diameter tubes, as a result of curvature effects [12]. Only the armchair structure results in truly metallic behaviour, while in other quasi-metallic SWCNT chirality dependent band gaps in the range of meV arise at low temperature [23]. The electronic structure yet is independent on the handedness and therefore identical for the mirror image of a nanotube structure.

2.2 Expectations from reported systematic Kataura Plots

Now we want to make use of the main insights so far. We know the quasi one-dimensionality of SWCNT gives sharp and intense electronic transitions [24]. The density of states (DOS) is dominated by van Hove singularities (vHSs) due to confinement along the circumference of the nanotubes and thus quantization of electronic and phonon states occurs [23]. The optical and spectroscopic phenomena are owned to transitions between those singularities, which makes the analysis of underlying experiments convenient. The distance between two neighbouring allowed k-values or cutting lines in figure 4 is connected to the SWCNT diameter by $\Delta k = 2/d$. This leads to an inverse proportionality of the distance between vHSs as well. The vHSs above and below the Fermi level result from k-values closer to the Dirac point in the BZ. The band diagram gives

cones, i.e. a roughly linear dependency on k, close to the Dirac points. For a specific (n,m) SWCNT with the set of vHSs, there is a set of transition energies E_{jj} from the electronic valence to the conduction band with a corresponding symmetry. The linear dependency holds for low energy transitions E_{jj} and is convenient for optical experiments with semiconducting SWCNT.

$$E_{jj} = \frac{2j\sqrt{3}a\gamma_0}{d} \tag{7}$$

The depiction of E_{jj} energy in dependence of the diameter is referred to as Kataura Plot and is an important guideline to investigate SWCNT properties. The notation is consistent as introduced beforehand. To remember, the index j is an integer and precisely a multiple of 3 for SWCNT with metallic behaviour. Computation of van Hove Singularities by parametrized model calculations, i.e. tight binding approximation is extremely helpful, but gradually also spectrofluorimetric data accomplish tables for isolated (n,m) structures.

Experimental researchers constructed Kataura Plots from single-walled carbon nanotubes in aqueous suspension empirically, which predict optical transitions for more than one hundred (n,m) structures, see figure 5. Filled dots in the plot represent experimentally obtained data points, whereas hollow points depict extrapolated values beyond the measured range of 0.62nm to 1.41nm. The empirical formulas used for extrapolation reproduce the experimental findings with an average error of 1.3meV for E_{11} and 5meV for E_{22}. The experimental investigations are based on these reported values in the literature as the average errors between the experimental data and the systematic fitting could be reduced by approximately 40% in comparison to tight binding model-based approaches [25]. The first and second optical transitions for the semiconducting SWCNT investigated hereby are shown in table 3 and are especially highlighted in figure 5. The expected second van Hove transition energies span the visible range from 537nm (2.307eV) to 722nm (1.716 eV). Seven excitations are available in the Raman laboratory, see section 3.2. As the second optical transition reported for the (6,5) structure $\lambda_{22} = 566nm$ is very close to an available laser excitation wavelength of $\lambda_{exc} = 568nm$, this is a preferential candidate to test the systematic measurements with the equipment. Although there is no explicit data for the left-handed enantiomer M-(6,5), the response for the sample is expected to be similar for the above explained reasons. Moreover, the (10,3) structure is expected to be close to resonance for laser wavelength $\lambda_{exc} = 633nm$.

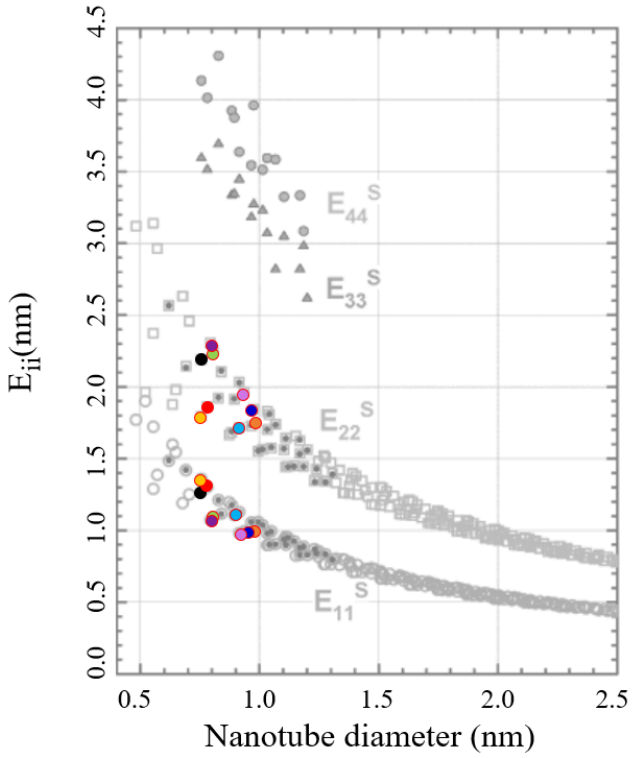

Figure 5: The empirical Kataura plot shows optical transition energies versus diameter for more than one hundred nanotubes. Experimental data is shown as filled points, whereas extrapolated data is depicted hollow. The investigated structures are highlighted in colour. The colour value can be found in table 3 and is consistent throughout the thesis. The data is adopted from [25].

Table 3: First and second optical transitions in units of eV as well as nm for easy comparison with laser wavelengths. Listed is the data for the investigated (n,m) structures from reference [25]

colour	(n,m)	d (nm)	θ (deg)	mod[n-m,3]	λ_{11} (nm)	E_{11} (eV)	λ_{22} (nm)	E_{22} (eV)
black	(6,5)	0.757	27	1	976	1.270	566	2.190
red	(8,3)	0.782	15.3	2	952	1.303	665	1.863
orange	(8,6)	0.966	25.28	2	1173	1.057	718	1.727
yellow	(9,1)	0.757	5.21	2	912	1.359	691	1.794
green	(9,2)	0.806	9.83	1	1138	1.090	551	2.251
light blue	(9,4)	0.916	17.48	2	1101	1.126	722	1.716
dark blue	(9,5)	0.976	20.63	1	1241	0.999	672	1.845
violet	(10,0)	0.794	0.00	1	1156	1.073	537	2.307
pink	(10,3)	0.936	12.73	1	1249	0.993	632	1.963

2.3 Towards high purity single chirality carbon nanotubes

To elucidate the complete intrinsic properties of SWCNTs and advance their applications, highly purified single-structure (n,m) CNT with a narrow diameter distribution are of high interest. Sorting methods based on electrical character, length, diameter, chirality and/or handedness make progress by various approaches. One can distinguish preferential synthesis, selective destruction and post-synthesis selection like ultracentrifugation, chromatography and aqueous two-phase extraction. The research development is represented in an exponential rate of journal publications concerning sorted CNT in the last decade reported by the Web of Science database [12]. The challenge of nanotube fabrication with a high purity in helicity as well as handedness is focused by scientists. Moreover, the post-synthesis selection methods made big steps towards sorting of helicity and handedness simultaneously in recent research [19]. Thereby, the control over selection of left-handed and right-handed CNT can be achieved using single-stranded DNA. Defined and ordered structures of short-stranded DNA with palindrome symmetry form distinct folds on CNT enantionmers. Together they resemble a macro-molecule of DNA-wrapped CNT, which shows distinguishable fluorescence intensity and chemical reactivity for the pairs of handedness.

Gel column chromatography is a second method, which effectively separates the optical isomers of SWCNT. It utilizes the different mobility of the isomers in an employed gel as the matrix. Gel based on allyl dextran has chiral moieties, which bound nanotubes with a specific handedness and let the other migrate through [11]. Based on the same principle is the multicolumn gel-chromatography, which as implied in the name, is conducted from a series of connected gel columns. A SWCNT dispersion is filled on the top column until the adsorption sites of the column are completely occupied by those nanotubes, which interact the strongest with the matrix. The nanotubes with different chirality are unbound and flow to the next vertically connected column, this is called the overload effect. In the next stage, the nanotubes with the second strongest interaction with the gel are adsorbed and so on, as illustrated in figure 6. Both techniques promise to allow the preparation of macroscopic amounts of single-structure nanotubes at low cost and high efficiency. As the control of distribution is limited in fabrication, characterization techniques such as Raman scattering is crucial.

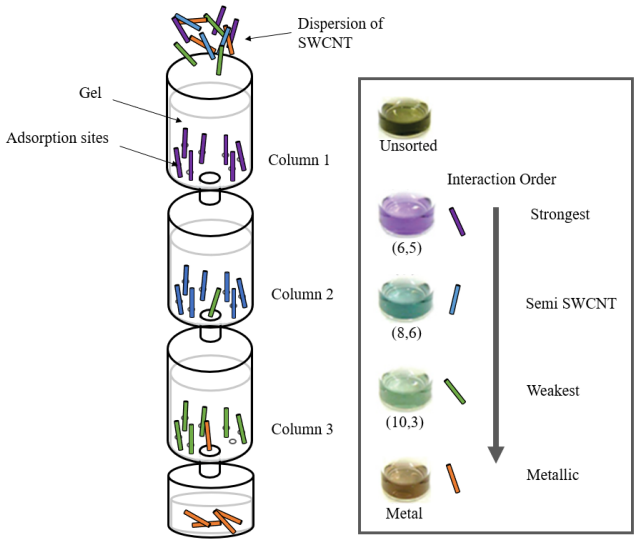

Figure 6: Illustration of the working principle of multi-column gel-chromatography, which is the method used to produce the monostructural SWCNT samples investigated in this thesis. The typical colour and the interaction order depending on the type are shown as an inset for three of the ten semiconducting probes. The figure is based on reference [14] with modifications.

2.4 Method related fundamentals

The investigation of our material candidate SWCNT by Raman scattering experiments offers a great potential to understand the structure, opportunities and challenges [26]. The actual goal of this chapter is to provide the essential background to understand the choice, as well as interpret the results, of the chosen experimental method.
The description of the background is mainly influenced from the references [23, 27], unless otherwise stated.

2.4.1 Description of Raman scattering process

Raman typically utilizes intense UV-vis incident light ν_0 to irradiate a sample and observes scattered light usually in backscattering mode with a confocal setup. The light is scattered in all directions and includes photons proceeding from Rayleigh ν_0 and a small fraction (approximately 1 in 10 billion photons) from Raman scattering $\nu_0 \pm \nu_m$, where ν_m is a vibrational frequency. The Raman effect is based on inelastic scattering of light when hitting a material. A schematic illustration of the Raman process and its difference to Rayleigh scattering is illustrated in figure 7. Due to the energy conservation during the rarer process the material loses or gains energy from the interaction, giving rise to the Stokes or Anti-Stokes line in a Raman spectrum respectively.

- Stokes shift occurs if an incident photon transfers part of its energy to the molecule and it is frequency-shifted towards lower energy. The probed material absorbs the energy to undergo transition to a higher vibrational state.
- Anti-Stokes shift occurs when an electron in an excited vibrational state transfers energy to the incident photon, resulting in a transition to a lower state or to the ground state. The scattered photon is frequency-shifted to higher energy. The Anti-Stokes lines show lower intensity in comparison to the former, because excited states are weaker populated than the vibrational ground.

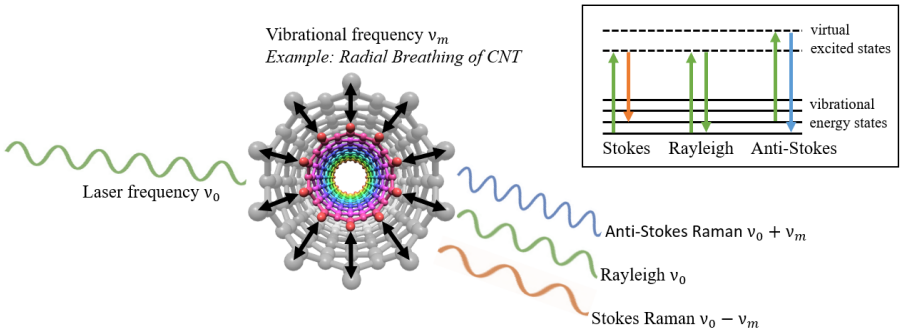

Figure 7: Rayleigh, Stokes and Anti-Stokes Raman scattering illustrated schematically. The inset shows an energy level diagram (Jablonski diagram) showing the states involved in Raman spectra. The figure is based on reference [28] with modifications.

The difference in energy between the incident photons and inelastically scattered photons is called Raman shift. A plot of the intensity of the inelastically scattered light as a function of the energy change is called Raman spectrum. Besides the common physical principle behind spectrometers of dispersion with a diffraction grating, one can find the spectrum without spreading the beam into wavelengths. In the model of light as a time-varying electromagnetic field, the power is proportional to the square of the field. Then the spectrum can be calculated as the magnitude of the Fourier transform of the power.

2.4.2 Background and notation in the classical manner

Raman spectroscopy belongs to the field of vibrational spectroscopy and it uniquely characterizes a molecule by the frequency, intensity and shape of the associated bands. In other words, the vibrational energy levels depict a fingerprint of a specific molecule, determined by the present atom masses, their relative arrangement in space and chemical bond strength. The Raman signal

therefore indirectly displays the specific structure, by inelastic light scattering.

This process is based on a change in polarizability α_0 by the quasi-particles. In other words, it is a measure for the distortion of an electron cloud by an applied electric field. An incoming electromagnetic wave, i.e. an applied field $\vec{E}(w) = \vec{E_0} cos\omega t$, changes the polarizability α_0 of the structures orbitals. The angular frequency is $\omega = 2\pi\nu$ and E_0 is the amplitude. The influence is leading to an electric dipole moment in the form of $\vec{P_D}(\omega) = \alpha_0 \vec{E}(\omega)$, which causes a periodic deformation and hence, the molecule vibrates with a characteristic frequency (McCreery, 2000). Moreover, as the polarizability depends on the distance and orientation between the orbitals, a vibration of the molecule with frequency Ω leads to a periodic modulation represented in the term of α_1. Hence, the total dipole moment $\vec{P_D}(\omega)$, including the influence of an external field $\vec{E}(\omega)$ and a vibration of Ω, can be described by equation 8.

$$\vec{P_D}(\omega) = (\alpha_0 + \alpha_1 cos\Omega t)\vec{E_0} cos\omega t \tag{8}$$

The outgoing electromagnetic wave therefore shows oscillations at the frequency of ω and oscillations shifted by $\pm\Omega$. Because the vibrational frequencies are of the magnitude of few cm^{-1} and α_1 is typically small compared to α_0, the incoming light needs to be efficiently suppressed in order to measure the sidebands. For periodic phonon structures in a crystal lattice interference leads to coherently and incoherently scattered light according to Bragg's law, see equation 9. The orientation of the scattered light relative to the incident beam is given by the angle θ and is defined by the wavelength of the phonon Λ and the wavelength of the incoming light λ.

$$2\Lambda sin(\frac{\theta}{2}) = n\lambda \tag{9}$$

As a consequence, to describe the case of crystals we use a 3x3 dimensional Raman tensor derived from the susceptibility tensor χ_{jl} instead of the scalar polarizability α. The components of the Raman tensor $\chi_{jl,k}$ are obtained as the derivation of the susceptibility tensor entry with respect to the 3N-3 normal coordinates Q_k as in equation 10. The indices j and l correspond to the three dimensions and the index k runs over the vibrations of N atoms per unit cell.

$$\chi_{jl,k} = \frac{\delta\chi_{jl}}{\delta Q_k} \tag{10}$$

In general, for a given molecule with N atoms the degrees of freedom (DOF) are categorised in translational, rotational and vibrational forms. We describe the translation with three DOF, for example with cartesian coordinates $\vec{x}, \vec{y}, \vec{z}$. Then we can rotate the molecule around three axis, so three rotational DOF, unless we have a linear system, then we have only two non-trivial rotations. So we expect a number of 3N-6 vibrational degrees of freedom, or 3N-5 for linear systems (Smith and Dent, 2005). However, not every phonon is Raman active. The symmetry of the atoms positions to each other is determining the

role of the phonon, i.e. when the displacements compensate their particular impact we say the oscillation is inactive or silent. Group theory predicts which phonon species in the different point groups results in vanishing Raman tensor components. An intuitive example are point groups with inversion symmetry, the compensation mandates that all vibrations are either Raman *or* infrared inactive. The scattering intensity is proportional to the square of the Raman tensor, but it is convenient to change to the quantum mechanical representation to demonstrate the explicit intensity. We distinguish longitudinal (LO) and transverse (TO) optical mode components in dependence of the displacement direction relative to the phonon wavevector $\vec{q}$, which can influence the necessary scattering symmetry choice.

2.4.3 Raman intensity and the quantum mechanical notation

It is crucial to understand the quantum mechanical origin of scattering processes for the explicit calculation of Raman intensity. Upon the excitation of an excited electron to state n, it can relax back to $0, 1, 2, ...n-1$, where the transition back to the prior state is known as Rayleigh and for others one gets Raman scattering. This energy difference is referred to as Raman shift, typically translated to wavenumbers and given in cm^{-1} [29]. The theoretical background is key knowledge for a correct interpretation of Raman measurements. Raman scattering is always a combination of two electron - photon interactions, resulting in inelastically scattered light, which we can probe and analyze relative to the incident beam. In particular, an electron is excited to the conduction band by absorption of a photon, there scattering occurs by emission (Stokes) or absorption (Anti-Stokes) of a quasi-particle (most frequently optical phonons), and it recombines back to the valence level under emission of a photon. The interpretation of the sidebands we obtained before is emission of a phonon for positive shifts (Stokes) and absorption for negative shifts (Anti-Stokes).
A materials energy structure consists of purely electronic levels, superimposed by vibrational and rotational levels, which are referred as the corresponding energy manifold. The rotational fine structure occurs in the gaseous phase for small molecules, while in the solid-state inter-molecular interactions restrict the molecular rotations. Vibrational transitions can be observed with either infrared or Raman spectroscopy. In the former, the absorption of infrared light as a function of frequency is governed by the Beer-Lambert law. However, Raman spectroscopy stems from coupling of an external electric field with the energy levels of the *bonds* between atoms. Such a vibration is commonly illustrated by two atoms as masspoints and a bond acting like a spring connecting them. The energy levels in a bond can be described by the quantum harmonic oscillator model, although it lacks to describe the formation and dissociation of the bond. To describe a bond break with internuclear separation, the asymptotic behaviour approaching the dissociation energy in the Morse model[1] exceeds the

[1]The Morse potential $V(r) = D_e(1 - e^{-a(r-r_e)})^2$ with width parameter $a = \sqrt{\frac{k_e}{2D_e}}$ takes into account the formation and dissociation of a bond between two atoms. It reaches its

characteristic parabola shape centered at the equilibrium distance between the atoms. However, in principle the quantum harmonic oscillator (QHO) is the simpler model and we are not interested in those extreme cases anyways. Decreasing the distance leads the bonding energy to infinity, due to the nuclear forces. Only definite energy levels, i.e. vibrational levels are allowed. The separation between the energy levels is given by $\hbar\Omega$.

In order to discuss the Raman process we need the susceptibility matrix element for the transition from the initial state i to the final state f, similar to the classical description. Accordingly, the transitions are induced from a dipole moment resulting from an applied electric field, transformed into the bra ket formalism we obtain equation 11.

$$\mathbf{P_{fi}} = \langle f|\mathbf{P}|i\rangle = \langle f|\epsilon_0\chi\mathbf{E}|i\rangle \tag{11}$$

The transition matrix element in this formalism is calculated by an integration over all spatial X and electronic x coordinates, because $\langle f|$ and $\langle i|$ are generalized wavefunctions. From this equation the transition susceptibility matrix element can be extracted, under the approximation that the phonon wavelength is much smaller than the probing lights wavelength ($\Lambda \ll \lambda$) and the adiabatic approximation [2]. Under the stated approximation for the wavelength the electric field E is assumed constant [27] and we can proceed with the relevant parts for the integration.

$$[\chi_{jl}]_{fi} = \langle f|\chi_{jl}|i\rangle = \int \rho_f^*(X)\phi_f^*(x,X)\chi_{jl}\phi_i(x,X)\rho_i(X)dxdX \tag{12}$$

The susceptibility in this form depends on the nuclear coordinates X and the electron coordinates x, hence it is characterised by the electronic orbitals of a specific material. We integrate over all electron coordinates and introduce normal coordinates Q_k in analogy to the classical notation. Subsequently, we can do a Taylor expansion of χ_{jl} with respect to Q_k, considering only the linear term, and extract the expansion coefficient from the integral. The product of harmonic oscillator wave functions with the occupation numbers ν_{fk} and ν_{ik} yields the total vibrational wave functions. We get:

$$[\chi_{jl}]_{fi} = (\chi_{jl})_0\langle ...\nu_{fk}...|...\nu_{ik}...\rangle + \sum_k (\frac{\delta\chi_{jl}}{\delta Q_k})_0\langle ...\nu_{fk}...|Q_k|...\nu_{ik}...\rangle \tag{13}$$

Due to the orthogonality of the wave functions, the first term in equation 13 vanishes for all cases mixtures of wave functions. Only when the quantum state is unchanged $\nu_{fk} = \nu_{ik}$ for all k it is valid, which describes the process of absorption or Rayleigh scattering. The second term is including the derivation of the susceptibility tensor and it is responsible for the Raman scattering process.

asymptotic limit at the dissociation energy with increasing inter nuclear distance.

[2] "A physical system remains in its instantaneous eigenstate if a given perturbation is acting on it slowly enough and if there is a gap between the eigenvalue and the rest of the Hamiltonian's spectrum" from M. Born and V. A. Fock (1928)

Considering again the orthogonality of the wave functions, we obtain that it is nonzero when $\nu_{fk'} = \nu_{ik'}$ for all modes $k^{'} \neq k$ and $\nu_{fk} = \nu_{ik} \pm 1$ for mode k. The Stokes and Anti-Stokes Raman process in the quantum mechanical picture yields equation 14 and equation 15 respectively.

$$[\chi_{jl}]_{\nu_{ik}+1,\nu_{ik}} = (\nu_{ik}+1)^{1/2}\sqrt{\frac{\hbar}{2\Omega_k}}\left(\frac{\delta\chi_{jl}}{\delta Q_k}\right)_0 \tag{14}$$

$$[\chi_{jl}]_{\nu_{ik}-1,\nu_{ik}} = (\nu_{ik})^{1/2}\sqrt{\frac{\hbar}{2\Omega_k}}\left(\frac{\delta\chi_{jl}}{\delta Q_k}\right)_0 \tag{15}$$

The intensity depends on the vibrational occupation number ν_{ik}. Therefore, thermal averaging is necessary with the help of the Boltzmann factor[3], which gives $n_k + 1$ for Stokes and n_k for Anti-Stokes. Herein, n_k is the Bose-Einstein distribution (equation 16) for the vibrational mode k oscillating with frequency Ω_k.

$$n_k = f_E(\Omega_k) = \frac{1}{exp(\hbar\Omega_k/k_BT) - 1} \tag{16}$$

Thus, the scattering intensity per unit solid angle can be evaluated. Intensities are rather given as radiance in watts per steradian, than in watts per area. In this description the Raman scattering intensity I is proportional to the square of the Raman tensor, which components are the elements $(\chi_j l)_k = \frac{\delta\chi_{jl}}{Q_k}$. Special focus is put on the E_{11} and the E_{22} transition energies and the matrix elements χ_{ii} includes optical absorption, electron-phonon coupling and emission. The maximum Raman intensity of a mode k with energy E_k is determined in the simplified model, neglecting many-body effects and excitons, in dependence of the incident energy E_{exc} by equation 17.

$$I(E_{exc}) \approx \frac{|\chi_{ii}|^2}{|(E_{exc} - E_{ii} - i\Gamma)(E_{exc} - E_k - E_{ii} - i\Gamma)|^2} \tag{17}$$

The value of Γ depends on the decay mechanism of the excited quasiparticles, it describes the full width at half maximum (FWHM) of the Raman lines. The theoretical lines are of Lorentzian shape, commonly overlapped by a Gaussian profile from the width of the laser line. The apparent width of the laser is defined by the finite resolution of the spectrometer. In particular it is a "scattering rate", inversely proportional to the lifetime of the phonon state, which are temperature dependent [30]. It is a broadening factor for the resonance range and accessible via Resonance Raman spectroscopy studies [31]. From the intensity equation it is evident that there are two maxima, originating from the resonance conditions in the denominator. Either the excitation energy matches the transition energy or the energy of the scattered light. In Resonance Raman scattering (RRS), the incident lasers energy is adjusted to coincide with the conditions found in equation 17. The incoming resonance is met when the incoming

[3]The thermal averaging is determined by $\sum_{\nu_k}(\nu_k + 1)W(E_k)$, where $W(E_k)$ is the probability to have a mode k with energy $E_k = \hbar\Omega_k(\nu_k + 1/2)$ in the QHO model.

excitation photon energy fits the nanotubes optical transition, whereas outgoing resonance occurs if this applies for the inelastically scattered photon. The difference between the wavevectors for those photons is the Raman shift given in cm^{-1}. In RRS intensity is further enhanced by the large density of electronic states (DOS) available for the optical transitions. This large density of states is especially important for one-dimensional systems, which have singularities in their density of states at the energy onset of an allowed optical transitions. The resonance of the RBM and G line from Raman excitation profiles (REPs) are found to be strikingly asymmetric with a weaker outgoing resonance than the lower-energy incoming resonance [32]. This observation is irrelevant of the preparation method for the chirality-enriched specimen and the REP asymmetry is explained by quantum interference from phonon mediated state mixing between the light and excitons with momentum $k = K$ [32].

2.5 Carbon nanotube associated Raman spectroscopy

2.5.1 Important vibrational modes

A number of features in the Raman spectrum of SWCNT originate from certain phonon modes we can identify, which reflects much information about the electronic, phonon and hence molecular structure. The interpretation of Raman spectra and the assignment of the belonging molecular structure is conducted with the help of two main approaches [33]. First, a helpful approach is using group theory with mathematical calculations of the forms and frequencies of the vibrational bands. Whereas second, the study of group frequency analysis, where certain functional groups have empirical characteristic vibrations, mechanically independent and uncoupled of the remaining molecule. Likewise in carbon nanotubes there are characteristic scattering modes that dominate the spectrum, which results in a typical response as illustrated in 8. However, the handedness can not be identified using Raman spectroscopy, as both left- and right-handed enantiomers result in the same spectra [34]. The lattice dynamics and thus the phonon eigenmodes of SWCNT is in many regards similar to the one of graphene [35], the differences are also described in the following.

Radial Breathing Mode

The Radial Breathing Mode (RBM) is not present in the 2D allotrope graphene, it is unique for the tubular shape with a specific diameter of CNT and corresponds to the radial stretching and contraction. The RBM position typically lies in a range between $100cm^{-1}$ and $350cm^{-1}$ and its position is most commonly used to determine the diameter of (individual) tubes by

$$\nu_{\mathrm{RBM}} = \frac{A}{d} + B \approx \frac{234}{d}. \tag{18}$$

The formula might seem gratuitous and one finds a variety in literature, but the inverse proportionality to the diameter is beyond doubt. The A value in the numerator stems from the velocity of the longitudinal mode [36] and B stems

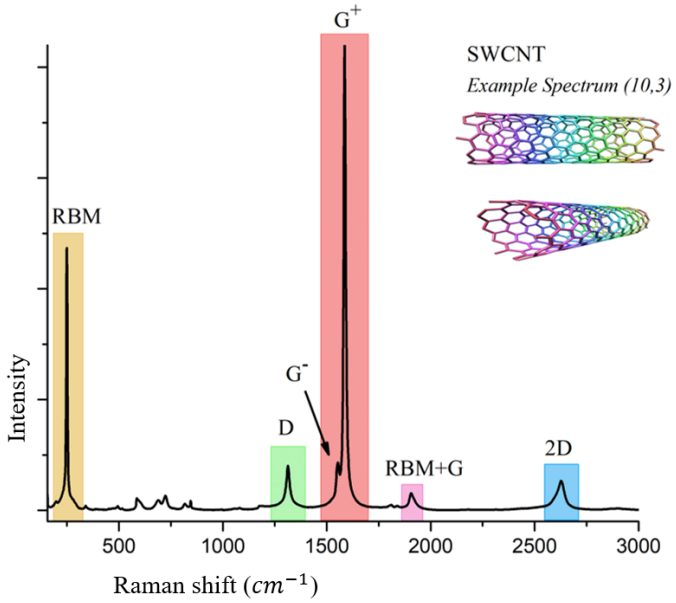

Figure 8: Representative example of a Raman spectrum with the characteristic modes for single-walled carbon nanotubes SWCNT highlighted and labelled. The inset shows a model of the corresponding structure (10,3) from two perspectives.

from environmental effects and can shift the RBM up to $18cm^{-1}$ [37]. Investigations on molecular dynamics propose an upshift in the RBM frequency between 4 and $10cm^{-1}$ for low-diameter SWCNT immersed in H_2O. The dominating process therefore was the dynamic coupling with the solvation shell [37]. It is endorsed to use equation 18 for isolated SWCNT, in contrary to $A = 234$ and $B = 10$ wavenumbers for bundles of SWCNT [38]. As a possible frequency shift of the dried droplets versus SWCNT in aqueous solution will be evaluated, the B value is set to Zero. In many cases, a weaker overtone is observed where RBM frequency is added to the G mode frequency at $\nu_{RBM+G} \approx 1750cm^{-1}$, which however are not taken into consideration during the interpretation of the spectra.

G mode

The designation of the G mode stems from the prime letter of graphite and it corresponds to planar vibrations of carbon atoms. Thus, it is characteristic for all sp^2 hybridized carbon systems and originates from the C-C bond stretching. For SWCNT in comparison to graphite the G mode is red-shifted and separated into a G+ and G- peak, which are a result of the longitudinal (LO) and circumferential (TO) stretching of the tube respectively. Herein, the circumferential

expansion contribute to a lesser extent, which results in a weaker G- peak signal. The relative intensities can be used to estimate the diameter and type of the nanotubes. The TO stretching component is shifted towards lower energy with decreasing diameter. The G mode in SWCNT is frequency shifted to localize between 1560 and 1620 wavenumbers.

D mode

The D band originates from photon-defect interaction of structural defects in carbon allotropes. It originates from in-plane breathing of the hexagonal carbon bonds. The coupling of excited electrons with wave vector k occurs commonly for vibrational modes with with $q = 2k$. The ratio between G and D mode intensities is a reporter of functionalisation, meaning structural quality of SWCNT. Especially high-quality samples of SWCNT show D mode intensities lower than one percent of the G band maximum. In an ideal nanotube the D mode vanishes as it is induced by a structural defect. It is dispersive, meaning its frequency depends on the excitation wavelength, see table 2.5.1.

2D mode

The 2D band is the second overtone of the defect-induced D mode and thus is located at double frequency. It includes two transverse optical (iTO) phonons at the K point. It does not require a defect state, but involves a pair of phonons that cancel the momentum with $+q$ and $-q$, leading to a stronger intensity. The spectral position of the 2D mode depends on the diameter as well and can give a hint on the sample type. The second K-point phonon ensures the momentum conservation and it is also dispersive with shifts of $106cm^{-1}$ per eV shift of excitation [23]. However, a recent study on the double-resonance Raman spectra in single-chirality-enriched SWCNT shows that a series of *non-dispersive* D and 2D Raman peaks arise [39].

The optical modes taken in consideration are listed in table 2.5.1 with their relevant characteristics for better comparison. The classification is defined by SR: single resonance, DR1: one-phonon double resonance and DR2: two-phonon double resonance. In other words, as stated above, double resonance means the excited electron with k couples with a quasi-particle of wavevector $q = 2k$. The frequency is given at $E_{exc} = 2.41$eV if the mode is dispersive. The dispersion is defined as the change in phonon frequency in cm^{-1} for a change of 1eV. The Raman active optical mode for graphite like structures G is at $1582cm^{-1}$, splits in two components for nanotubes as in the description.

Table 4: Most important SWCNT related optical modes, their typical frequency, classification and dispersion, i.e. dependency on incident laser energy. The table is based on Table1 from reference [23]

Mode	Frequency (cm^{-1})	Classification	Dispersion (cm^{-1}/eV)	Explanation
RBM	234/d	SR	0	Radial Breathing Mode, Radial expansion/compression
D	1350	DR1	53	Intervalley scattering, LO or TO mode with q = 2k
G^+	1590	SR	0	In-sheet vibrations along tube axis
G^-	1570	SR	0	In-sheet vibrations along circumference
2D	2700	DR2	106	Overtone of D mode

2.5.2 Advantages of Raman spectroscopy for SWCNT

Optical spectroscopy techniques make use of the geometry dependent properties such as electronic energy levels and phonon activity to determine the underlying structure. Such an assignment is based on two-fold information, experimental and theoretical data. In the case of Raman scattering the combination of phonon frequency and optical transition energies are relevant. A big advantage of optical methods is their non-destructiveness and that they are practicable for macroscopic amounts, which makes lab work much more convenient. Photoluminescence (PL) as another example of optical experiments demonstrates the diverse information gainable besides the assignment of (n,m) indices. With steady-state and time-resolved PL spectroscopy the electronic states, charge carrier dynamics, optical selection rules and more can be studied depending on the obtained chirality vector. Nevertheless, Raman scattering as the inelastic event between photons and matter, has advantages over PL [40].

- First, it can be performed for semiconducting carbon nanotubes *and* metallic ones, while PL methods are not useful for the lather.
- Second, for tubes with semiconducting behavior it can be performed in the visible wavelength range, where the second optical transition is located. Thereby, infrared (IR)-sensitive detectors are not essential.
- A further advantage is the resilience over the environment. Raman signal is robust in identifying nanotubes in various environment, whereas PL e.g. in bundles with present metallic nanotubes is quenched.

Regarding the last point, it is worth mentioning that the environment indeed can affect the phonons and optical transition levels of CNT. The comparison between the Raman signal from individual tubes versus a bundle shows, that their interaction leads to red-shifted optical transition energies [40]. Raman scattering is an established tool to investigate the optical properties of SWCNT.

Herein, only those tubes with a transition energy similar to the incoming laser get probed. The sensitivity can increase by a factor of 10^3 to 10^6 when operating at the resonance frequency of the sample molecule, i.e. matching the vHSs for SWCNT. The main disadvantage of RRS is the increased risk of fluorescence and photo-degradation of the sample due to the increased absorption of the energetically matching incoming laser light.

3 Experimental Method

3.1 Sample description

The above stated relevance of monostructured SWCNTs for both fundamental research and applications in electronics, lead to the important experimental analysis of the carbon nanotube samples, which were produced using gel-chromatography by the group of *Kataura et al.* [14]. In the described manner, ten different structure-enriched semiconducting nanotube types were separated and send in containers of 30ml aqueous solution. Herein, it is to mention that the concentration is not specified and that in general CNT are badly soluble in water due to their low polarity. The aqueous solution is dropcasted on a Silicon (Si) wafer, because this technique needs only small amounts of approximately $1\mu l$, it is easy to focus and the signal from the environment is known (at $521cm^{-1}$) and well separated from the typical Raman modes of carbon nanotubes. The ten single-chirality-enriched SWCNT under investigation are: (6,5), (8,3), (8,6), (9,1), (9,2), (9,4), (9,5), (10,0), (10,3) and M-(6,5). The characteristic colour of the (n,m) types reaches from violet to dark green, see figure 9. For most of the samples approximately $30ml$ were provided, but three exceptions motivated the choice of the preparation method. One can clearly discern a difference in the intensity of the colour between (6,5) and M-(6,5) with the bear eye. We will keep in mind that the latter is more translucent for the interpretation of the results. The distribution of carbon nanotubes was captured with 10x magnification by an optical microscope and camera. The material is distributed quite evenly across the droplet exemplified by figure 10 showing sample (10,0). On the top one can see the edge of the droplet, which serves as a frame to navigate across the sample. The darker areas contain clusters of carbon nanotubes, which arrange in needle shaped bundles in many cases. Shown as an inset is a carbon nanotube cluster with a magnification of 100x.

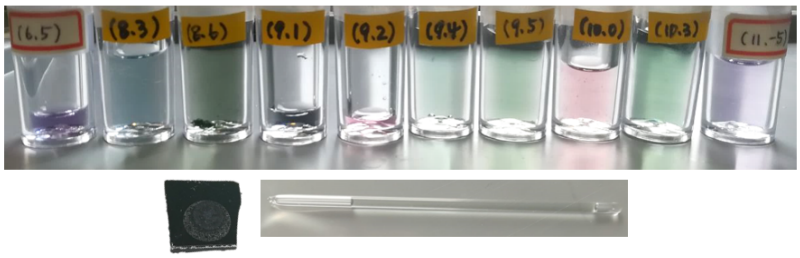

Figure 9: Picture of all containers including structure-enriched aqueous solution with the (n,m) labels. Below a depiction of a droplet on Si substrate and a capillary in original size.

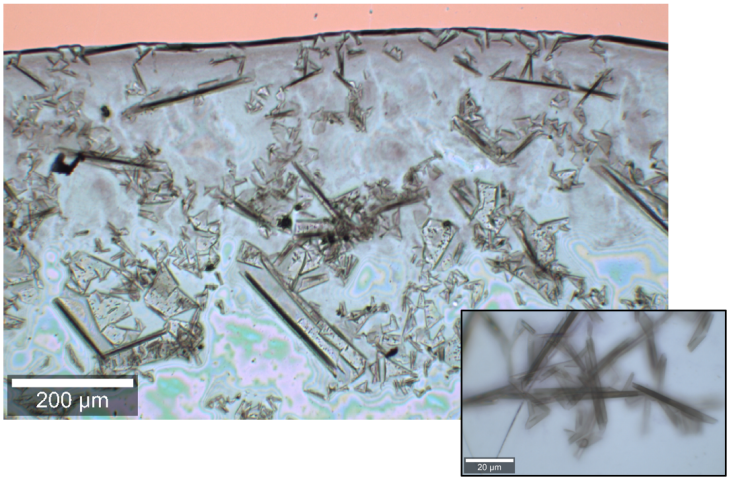

Figure 10: Picture of CNT distribution on dropcasted sample (10,0) with 50x and 100x (inset) magnification.

In addition to the dropcasted set, measurements are performed in liquid form to establish possible alteration of the electronic band structure due to interaction with the environment. The supports consist of a glass capillary filled with $2\mu l$ of solution and sealed at both ends with a Bunsen burner. The curvature of the capillaries surface makes a direct measurement inconvenient. Therefore, the supports are submerged in distilled water, that has a similar reflective index to glass. This procedure greatly enhances the signal, because it flattens the outer surface of the capillary for the laser rays. Yet, the diffusional movement in liquids and the transparency of the surrounding toughen the conditions to have a nice spot and focus in comparison to the beforehand method. To assist the focusing procedure a piece of Silicon was placed besides the capillaries, the laser was focused on that surface and then the sample was positioned in the centre. Noticeable is also the orientation of the capillary, it has to be placed perpendicular to the sample stage to collect the largest amount of light with the setup in the LabRaman as well as the triple monochromator Raman.

3.2 Experimental optical setup

3.2.1 Available methods

The investigation described in this Master thesis is conducted with three different Raman setups within the research laboratory of the group *Electronic Properties of Materials*. Moreover, a fourth Raman system, the WiTec alpha 300A at the *Faculty Centre for Nanostructure Research*, was utilized. Both are located at the Faculty of Physics, in the University of Vienna and the author appreciates that the facilities were available for the completion of a diverse, relevant and interesting Master thesis.

3.2.2 Systematic Raman provides the key experiments

The fundamental Raman measurements are performed using a HORIBA Jobin Yvon LabRam spectrometer with seven excitation wavelengths, between a range of 50 and 3000 cm^{-1} in ambient conditions. The optical power on sample is kept below $1mW$ for the solid state samples and below $3mW$ in solution, to ensure the measurement runs in a non-destructive manner and to avoid laser-induced photochemistry. The optical power is obtained with a Si photodiode from Thorlabs and has a relative accuracy higher than 99%, which is relevant because the power is used in data analysis for normalization. The LabRam uses a tunable laser system, applicable for seven wavelengths in the range from ultra-violet to near-infrared. It is a confocal Raman microscope with a laser spot size of approximately $1\mu m$. A Olympus LMPlanFl objective with magnification of 50x and numerical aperture NA 0.50 is used for the present micro-Raman setup in backscattering mode. After dispersing the spectrum with a diffraction grating a charge-coupling device (CCD) detects the signal. The detector is cooled to $-80°$ with liquid nitrogen during operation. A schematic illustration of the backscattering Raman setup is shown in figure 11.
The Argon-Krypton gas laser Coherent Innova 70C Spectrum is utilized, which provides seven different gas lines for excitation. The laser operates with the following excitation wavelengths, namely 458nm, 488nm, 515nm, 532nm, 568nm, 633nm and 647nm. Some of those are close to the E_{22} transition energy for one corresponding SWCNT type according to the upfront literature (see section 2.2). Obviously, these are the first combinations of laser line and chirality to expect a high response. The setup provides a camera mode and a manual XY-stage to check a sufficient location to focus the beam with a microscope objective of 50x. Yet, the final measurements setting is based on the maximum signal of the G-line. Moreover, as the samples were produced by another group at least three years ago and not characterized since, the resulting spectra, particularly the RBM position, is checked to validate the labelling of the containers.

The advantage of a further Raman system that operates in the IR is seized, the WiTec alpha 300A enables the excitation with a wavelength of $785nm$. From the theoretical findings of chapter 2.2 it is evident, that some nanotube structures are expected to have their E_{22} inter-band transition in this region. In a first attempt, the (9,4) type is placed in focus to investigate the maximum power before the beam spot burns with this system. The measurements are thereon conducted with a 100x objective and $5mW$ power at the WiTec. The system includes an imaging operation to screen the sample and focus a spot. The manufacturer promises a lateral resolution down to $1nm$ for the system. The Raman spectra from 100 to 2800 cm^{-1} are recorded with the WiTec using one second illumination time and 100 single spot repetitions. The general setup for both systems utilized is similar and a schematic picture of the main beam path is shown in figure 11.

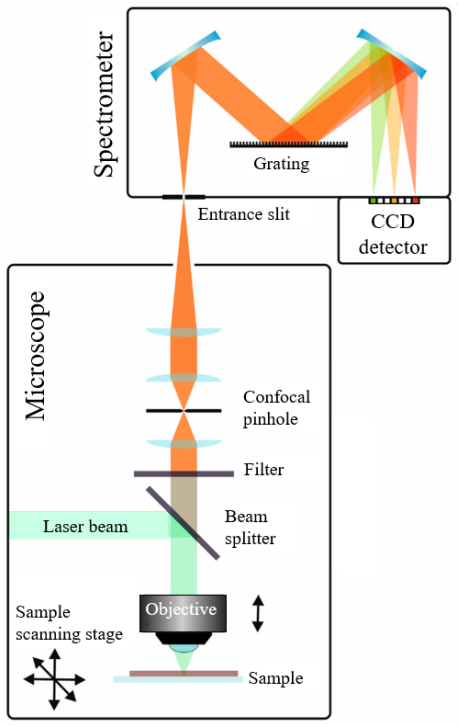

Figure 11: The optical setup of a typical Raman spectrometer in backscattering orientation. The figure is based on reference [28] with modifications.

The minimal detectable wavenumber shift between two pixels of the detector determines the resolution power of the Raman spectrometer. The backscattered light is dispersed by gratings and the density of nodes together with the illuminated area on the gratings transform to the resolution power in general. In our studies the Zero Point (Rayleigh peak) in wavenumbers is calibrated after every change in the setup and the laser line has a full width at half maximum (FWHM) of approximately $4cm^{-1}$ determining the uncertainty. That is because the entrance slit of illuminates more than one pixel, i.e. an entrance slit of $100\mu m$ corresponds to four pixels with $26\mu m$ width.

3.2.3 FTRaman

The Fourier Transform Raman spectrometer does not disperse the scattered light with a diffraction grating, but calculates the spectrum as the magnitude from the Fourier transform of the power. The FT spectrometer is a Michelson interferometer. Two beams that have passed through and reflected from a beam splitter superimpose and their interference gets detected. In one arm of the beam splitter there is a fixed mirror, whereas in the other arm is a mirror that moves with veloctiy v. For a stationary mirror, the coherent superposition of

two beams arrives in the output arm. The power depends on the phase delay between those beams in the output arm. If the length of the paths is such that the beams are in phase, then there will be constructive interference and a large signal. If the length difference between the two beams is an odd multiple of the half-wavelength, then the superposition will be destructive. For light incident at one wavelength, the output intensity will depict a sine wave with a period dependent on the wavelength and the velocity of the mirror. The spectrum of the source can be determined from the Fourier transform of the intensity. The FT Raman spectra for the whole set of dropcasted samples is gathered, while the capillaries can not be mounted in the sample holder.

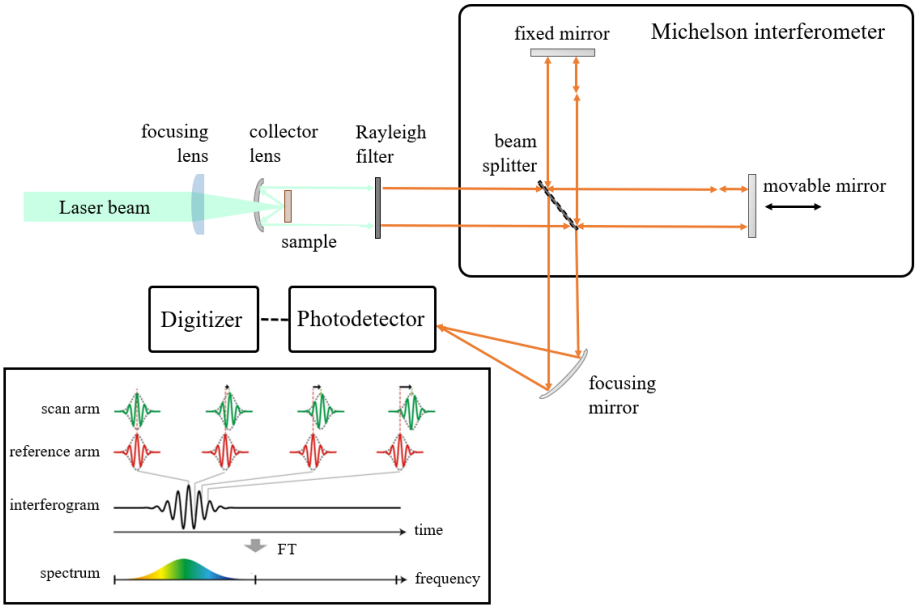

Figure 12: The optical setup of a typical Fourier transform Raman spectrometer. The inset depicts the compilation of the spectrum from the phase-shifted beams in the scan arm (movable mirror) and the reference arm (fixed mirror). The figure is based on reference [41] with modifications.

3.2.4 Triple monochromator Raman for resonance profiling

The system provides the advantage of a tunable light source with good spectral selectivity. It can operate with numerous chromophores, which determine the output wavelength over a large available range. Further laser output properties are specified from the present pump laser. This makes the whole setup very diverse. Herein, the optical resonator is a Radiant Dyes NarrowScan Laser pumped by a Q-switched Nd:YAG laser (EdgeWave GX-series). The Dye solution Rhodamin 6G in ethanol with a mass concentration of $\rho = 1\frac{g}{l}$ is put in

motion by a dye circulator (Radiant Dyes, type RD 1000). The pump emission lies at a wavelength of $\lambda = 532nm$ and the dye laser output wavelength is measured by a CCD spectrometer (AvaSpec-HS2048XL-EVO). The wavelength range of the used Dye is between 557nm and 584nm with a maximum efficiency of 30% according to the producers dyes specification, which can be found in the appendix. The optical power on sample is obtained with a Si photodiode *Thorlabs PM100D* and kept below $0.5mW$. Similar to the first setup an Olympus objective with magnification 50x is used in backscattering mode. The signal is dispersed by a *Horiba Jobin Yvon IHR320* spectrograph and detected using a photodiode *Horiba DSS IGA010L* at cryogenic temperatures.
For the determination of resonance profiles the excitation is varied in steps of $2nm$, embedding the wavelength we expect from the preliminary measurements. A broad resonance profile of more than tens of meV is an indicator for a distribution of nanotube diameters. Hence, the RBM and G line resonance is of high interest.

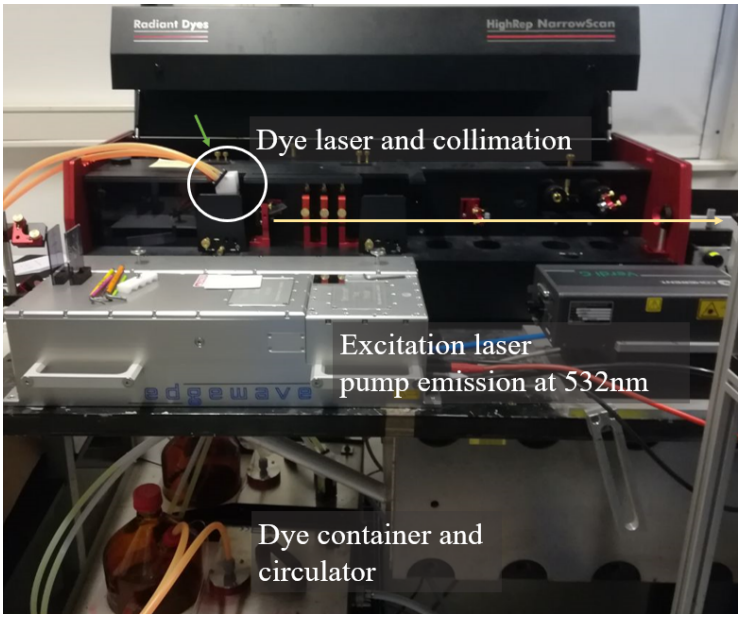

Figure 13: The generation of a tuneable light source with the Radiant Dyes NarrowScan Laser. The pump emission (532nm) is generated by a Q-switched Nd:YAG laser from edgewave. The pump beam excites the circulating dye at the white radiation chamber from the back of the picture, as indicated by the green arrow on the encircled position. The emitted light path is directed through collimation lenses from left to right and exits the laser as represented by the yellow arrow.

.

4 Results and Discussion

4.1 Analysis strategy of Raman spectra

Once the data treatment provides a nice overview of the Raman spectra as presented in section 4.2, we can resume to study them in relation to the formulated focus on enrichment and environmental deviations for the dropcasts.
The first research question:

1. Research Question: Do we observe environmental interactions or deviations in the Raman spectra of solid versus solution SWCNT?

is approached by a comparison of the resonant RBM frequencies ν_{RBM} as obtained from the LabRam measurements for both preparation methods. As explained in the theory section, frequency shifts due to environmental interactions can occur and are described by the parameter B in equation 18. A plot of the dropcast experimental value of ν_{RBM} on the ordinate versus the solution experimental value on the abscissa can therefore indicate a trend. If so, we can extract this information and discuss the frequency shift and its origin. The results are found in section 4.3.
Addressing the second research question:

2. Research Question: What is the stage of SWCNT post-synthesis selection by multi column gel-chromatography recently?

we use our findings to evaluate the enrichment in the single-chirality samples as introduced in section 4.4. This is approached by a comparison of the relative RBM Raman intensity for the set of samples. Each (n,m) SWCNT is associated with one dominant RBM, that must be close to resonance with one of the incident lasers. From the findings it is possible to conclude what specific structures are present (in accordance to the variety of excitations) and to what extend compared to the enriched (n,m) SWCNT. The results are presented in a stacked bar diagram showing the relative RBM composition in each sample and a further diagram for the defined relative modes in the various specimen.

4.2 Raman spectra

Processing of the data is systematic and joins the spectra belonging to each chirality for all available gas line excitations. The RBM, G line and 2D line range are shown, because they indicate the SWCNT properties. The full range plots from $150cm^{-1}$ to $3000cm^{-1}$ are found in the appendix A.2. The spectra are normalized for the G line to be height 1. Therefore, the number of resonant carbon nanotubes must be assumed to be proportional to the total amount of resonant carbon material contributing to the main G line. This normalization is chosen as it displays an intuitive first overview and to soften the absolute intensity uncertainty. Moreover, there is no information about the concentration of SWCNT in the solutions. What is known about the distribution of the

nanotubes in the droplets on Si is concluded from the pictures introduced in section 3.1. Additionally, the area of the G line signal per mW output power as measured with the photodiode is gathered in table A.3 in the appendix A.3. The usual Raman scattering signal is weak, but the scattering efficiency is enhanced when the excitation energy matches the transition energy between optically allowed electronic transitions in the material. The signal differs by a factor of up to 80 between the operation of different gas lines. In general, the signal to noise ratio is clearly sufficient even when normalizing spectra off resonance and near resonance to the same height.

The obtained spectra from the LabRam are gathered in figure 14 for the dropcasts. The first feature that attracts the attention are the multiple narrow peaks for the excitation with the NIR laser, shown as the black line in the two top most plots. They occur for wavenumbers higher than $2600cm^{-1}$ and were identified as fourth octave of H_2O from the surrounding air humidity. The vibrational bending motion of water is an optical mode with $> 330cm^{-1}$ [42]. They are seen irrelevant for the interpretation of the spectra regarding the SWCNT properties. The two top most plots show (6,5) and M-(6,5) for the varying exciting gas lines. They manifest their dominant RBM at $309cm^{-1}$ and $307cm^{-1}$ respectively, whose distinction is below our spectral resolution limit of $4cm^{-1}$. However, also a further feature arises at $282cm^{-1}$ while operating in the NIR (red and black curve), which is assigned to the (9,5) structure. A further example is the (8,3) type of SWCNT shown as the red line. It exhibits its E_{22} resonance in the NIR, yet a remarkable breathing mode arises when exciting with $515nm$. The corresponding RBM with $\nu_{\mathrm{RBM}} = 270cm^{-1}$ is again associated with another nanotube. Especially, the yellow excitation ($568nm$) yields an unexpected resonance for the whole set except for (6,5) and M-(6,5), which leads to a prominent RBM with frequency $\nu_{\mathrm{RBM}} = 242cm^{-1}$. The feature is not identified as one of the dominant modes for this excitation, which are the RBM of (6,5), M-(6,5) and (9,2), see figure 19. The diameter of the structure is evaluated as $234/242 = 0.967$ in nanometers. Following this argument, it could be (8,6) which has a reported diameter of $0.966nm$, but considering the resonance in the yellow it most probably is a nanotube type that is not covered in our set. This is the first indication for the presence of multiple nanotube types.

The experimental results from the IR Raman using the WiTec spectrometer are gathered separately, but presented together with the collection of spectra grouped by excitation, i.e. vice versa to previously, in figure 15.

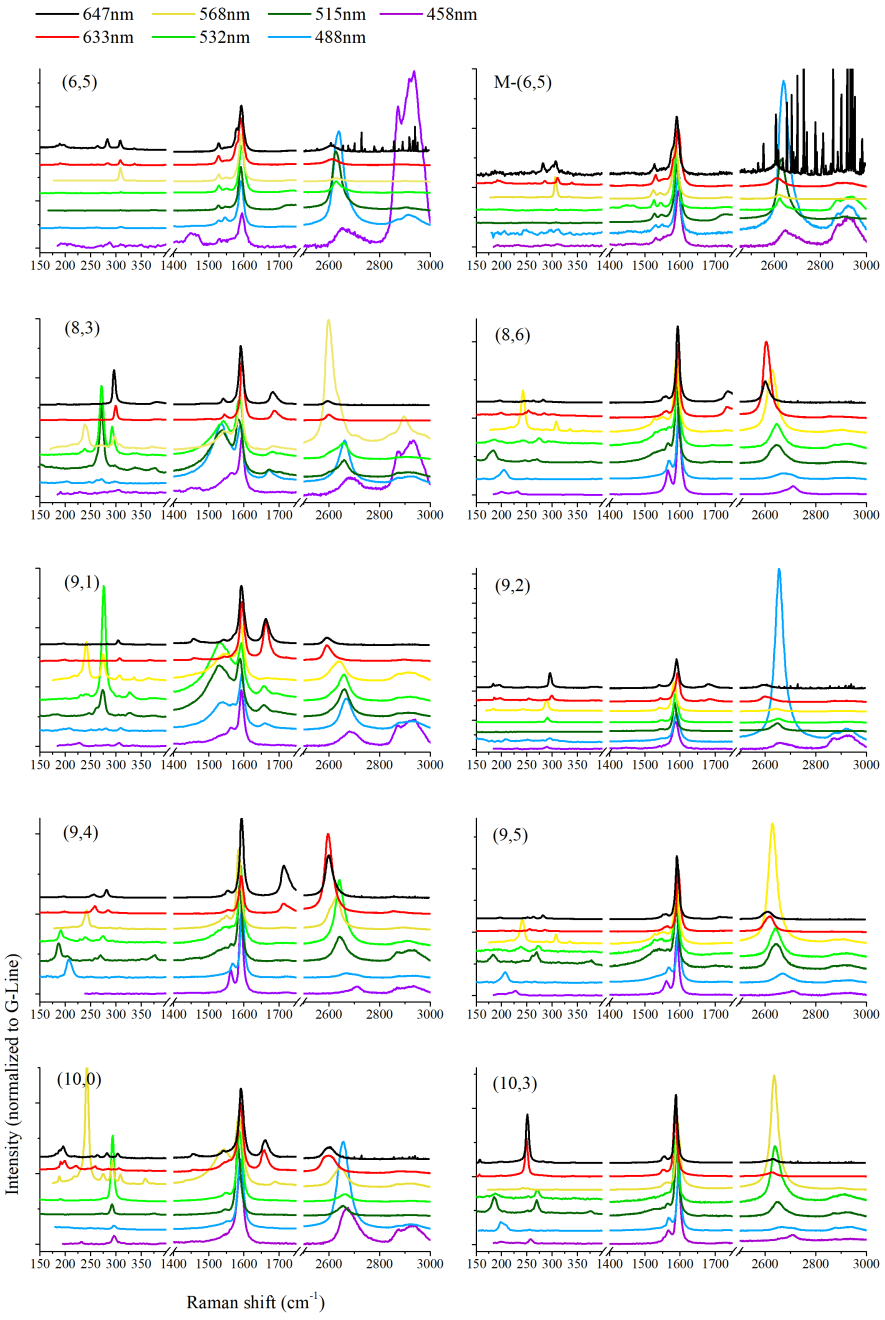

Figure 14: Dropcasted samples measured for seven excitation wavelengths λ_{exc} over the whole visible range using the LabRam system. The data is normalized to the G line and displays an overview of the various sample properties.

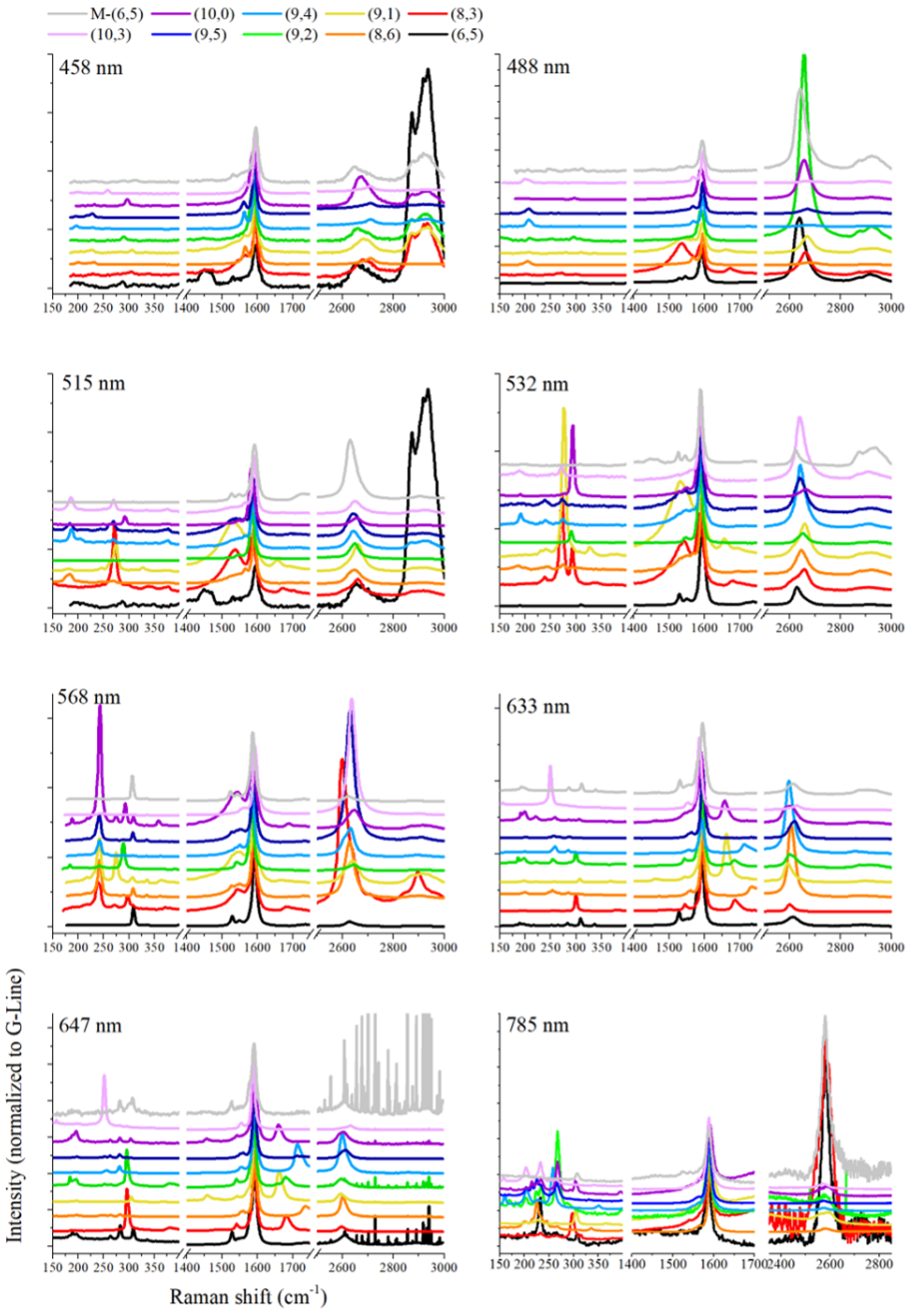

Figure 15: Raman spectra grouped by excitation, including the measurements at the WiTec IR Raman spectrometer at the bottom right corner. The resulting spectra are presented normalized to the G line in the RBM, G mode and 2D mode range.

The findings of the FT Raman measurements are shown in figure 16. On the left hand side, one sees the full measured range from the laser line at zero wavenumbers up to $3000cm^{-1}$. It is striking that the better the G line signal is, the stronger a periodic modulation of the background appears. The settings were absolutely identical for the samples and the spectrum for the bare substrate is included as well, which clearly depicts a constant. The origin of this sinusoidal characteristic is based on interference from sites with different layer thickness. The thicker the dropcast layer of SWCNT on the Si waver, the stronger the signal *and* the periodic background. As the operating laser energy for FT Raman lies typically in the infrared, the excitation is closest to the E_{22} transition energy of (9,4), followed by (8,6), (9,1), (9,5) and (8,3). On the one hand, the strongest signal is indeed coming from (9,4), but on the other hand, we observe deviations in the following resonance trend that probably stem from suboptimal laser spot positions. The FT Raman provides a live scanning mode to test the signal in x,y,z direction, yet only minor optimization was possible. The relative intensity of the D bands around $1300cm^{-1}$ seen in the Raman spectra are below 8% for all samples except (10,0), which demonstrates that most of the separated SWCNT contain only few defects. However, the FT spectrum for the (10,0) candidate spikes at $1278cm^{-1}$ with a relative intensity of 32% of the G line. Furthermore, there is a prominent peak for (10,0) and (9,2) at approximately $913cm^{-1}$, which is not belonging to an identified vibrational mode of SWCNT.

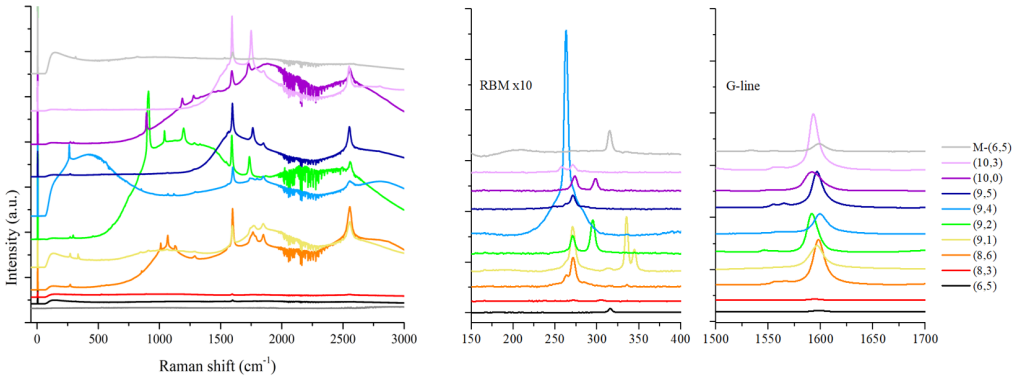

Figure 16: The Fourier Transform Raman spectra for the set of (n,m) candidates dropcasted on a Si wafer. The results are shown without background subtraction on the left. Herein, we observe a periodic modulation. The spectrum coming from Si only is shown as the grey line on the left for comparison. On the right hand side, the region of RBM and G line is illustrated.

4.3 Interaction with environment: dropcast and solution method

The comparison of the RBM position, from the samples in solution and the dropcasted counterparts will discern the interaction of individual tubes with the environment. Specifically, if the interaction is relevant to influence the electronic band structure. Therefore, the systematic Raman measurements using the gas laser are repeated for the second preparation method, see figure 17. However, the data for the solution in capillaries was normalized to the mW output power as measured with the photodiode, due to the distinctly lower total signal. The diffusive movement and particularly delicate focusing in a liquid was challenging the signal to noise ratio. The relative intensity between solid and liquid G line maxima $\frac{I_{G,solution}}{I_{Gdropcast}}$ was typically one third. The estimated signal as obtained with the LabRam is for instance 27% for sample (6,5) and $\lambda_{exc} = 568nm$ in comparison to the previous dropcasts. The multiplication factor to present the spectra in a grid with similar axis windows is shown as an inset below the (n,m) label. This spectra together with the results of the dropcasts are used to extract the relevant peak position.

Figure 18 shows the line position of selected strong RBM for the samples produced by the dropcasted method on the ordinate and for the aqueous solution on the abscissa. Obviously a linear dependency with a slope fixed to 1 is expected, whereas the intercept with the ordinate indicates a frequency shift. The calculated intercept parameter of a linear fit for the data is shown as an inset. The regular residuals of the fit are plotted on the right hand side. The intercept indicates a frequency downshift of approximately $-1cm^{-1}$ of the dropcasts compared to the liquid counterparts. Such a downshift of one wavenumber would come along with an increase in the transition energy in the magnitude of tens of meV. However, the relative standard deviation for the parameter of 35% is large and the residuals deflect from the fit in the same magnitude. Altogether, there is no significant frequency shift related to the drying process obtained. The evaporation does not result in a noticeable influence on the mode frequency. The aqueous solution of SWCNT commonly includes a surfactant to improve the solubility. The tensid forms a thin membrane around the nanotubes, which is most probably the local environment also after the evaporation of the solvent. The advantages of dropcasted samples mentioned in section 3.1 and the better signal to noise ratio make them a great alternative for the conducted experiments. The discussion on RBM composition and enrichment can be concluded from the results of the dried droplets. However, whenever a pulsed laser system is employed, the capillaries are the better choice, because they withstand the measurements without burning.

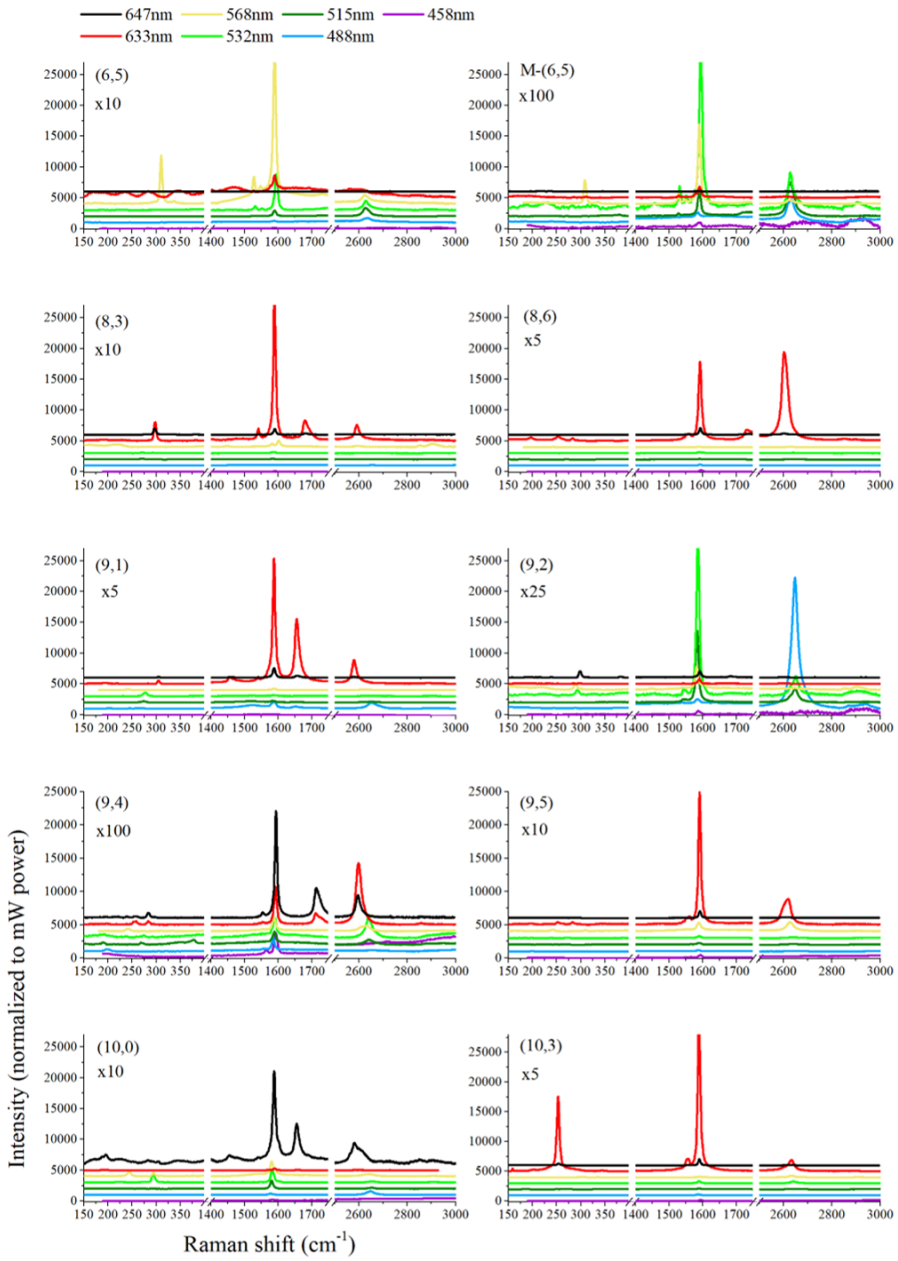

Figure 17: The Raman spectra for the investigated (n,m) structures in aqueous solution in the range of RBM, G-line and 2D line. Measured for seven excitation wavelengths λ_{exc} over the whole visible range using the Argon gas laser. The data is normalized to the mW power on sample and displays an overview and comparison for the most important vibrational modes of SWCNT.

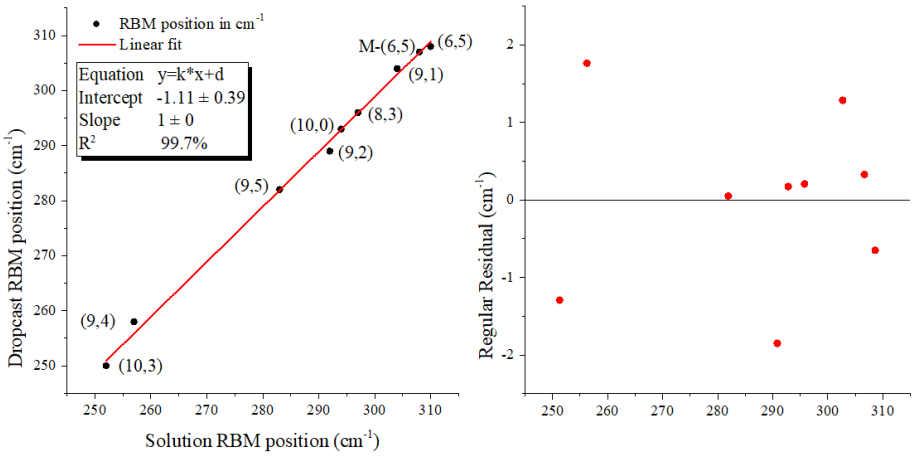

Figure 18: The Raman spectra for the investigated (n,m) structures in aqueous solution in the range of RBM, G-line and 2D line. Measured for seven excitation wavelengths λ_{exc} over the whole visible range. The data is normalized to the mW power on sample and displays an overview and comparison for the most important vibrational modes of SWCNT.

4.4 Enrichment of (n,m) structures

The colour difference in the various containers clearly demonstrates that SWCNT with different chirality were selectively adsorbed by the gel columns. The Raman spectra analysis for (n,m) enrichment is established by a detailed look to the RBM intensities. Already from the previous results in figure 14 it is clear that multiple RBM arise in resonance with different excitations. In the theoretical part we determined the background of resonance intensification by equation 17. The presence of tubes that are in resonance, result in an amplification of their signal by a factor up to 80 between the available gas lines. The sensitivity and selectivity of RRS makes it possible to investigate even trace amounts of specific chiralities.

The dominant breathing mode is defined as the RBM feature that represents the (n,m) type with enrichment. It is enhanced while operating the laser close to the resonance reported and the diameter is compared with literature values. However, the available lasers can not enhance all ten SWCNT types equally well. To illustrate which laser and structure combinations match, the enhanced signal is highlighted in table 4.4. Results from other combinations must be handled carefully, because the RBM affilliation can not be identified unmistakably. The table includes a list of the dominant RBM frequencies, the calculated diameters and a comparison with the corresponding values in literature. The diameter of the enriched species is based on equation 18. The presented A and B value

predict the diameter in accordance to the literature value with an average deviation of 4%. These small diameter SWCNT can be confidently assigned to their chirality. The $A = 248$ value proposed for individual SWCNT overestimates the diameter across the board. The resonant breathing mode in the spectra of all probes are gathered by excitation wavelength in figure 19. The following discussion on the enrichment is based on this plot. Once again, it is evident that the four samples (8,6), (9,1), (9,4) and (9,5) are not efficiently enhanced by any of the lasers, whereas the other samples clearly depict a dominant RBM as sketched as a vertical dashed line. The two samples enriched with (6,5) SWCNT, that have either right-handed or left-handed helicity, expose their RBM feature at $309cm^{-1}$ and $307cm^{-1}$ respectively. The difference is below the spectral resolution, hence we can conclude that both are congruent as expected.

Table 5: The experimental findings on the RBM frequency in comparison with the theoretical values adopted from section 2.2 are listed. The vertical line separates the theoretical and experimental elements. On the left, there is a column for the diameter, the E_{11} and E_{22} transition in units of wavelength and electronvolts. On the right, there is the excitation wavelength which depicts the highest resonance, the obtained RBM frequency and the diameter, which is calculated by $234/\nu_{\mathrm{RBM}}$. The sample structures that provide enhanced RBM signal by the laser with λ_{exc} are highlighted.

(n,m)	d (nm)	λ_{11} (nm)	E_{11} (eV)	λ_{22} (nm)	E_{22} (eV)	λ_{exc} (nm)	ν_{RBM} (cm^{-1})	d_e (nm)
(6,5)	0.757	976	1.270	566	2.190	568	309	0.757
(8,3)	0.782	952	1.303	665	1.863	647	296	0.790
(8,6)	0.966	1173	1.057	718	1.727	785	225	1.04
(9,1)	0.757	912	1.359	691	1.794	785	304	0.770
(9,2)	0.806	1138	1.090	551	2.251	568	289	0.809
(9,4)	0.916	1101	1.126	722	1.716	785	258	0.907
(9,5)	0.976	1241	0.999	672	1.845	647	282	0.830
(10,0)	0.794	1156	1.073	537	2.307	532	293	0.799
(10,3)	0.936	1249	0.993	632	1.963	647	250	0.936

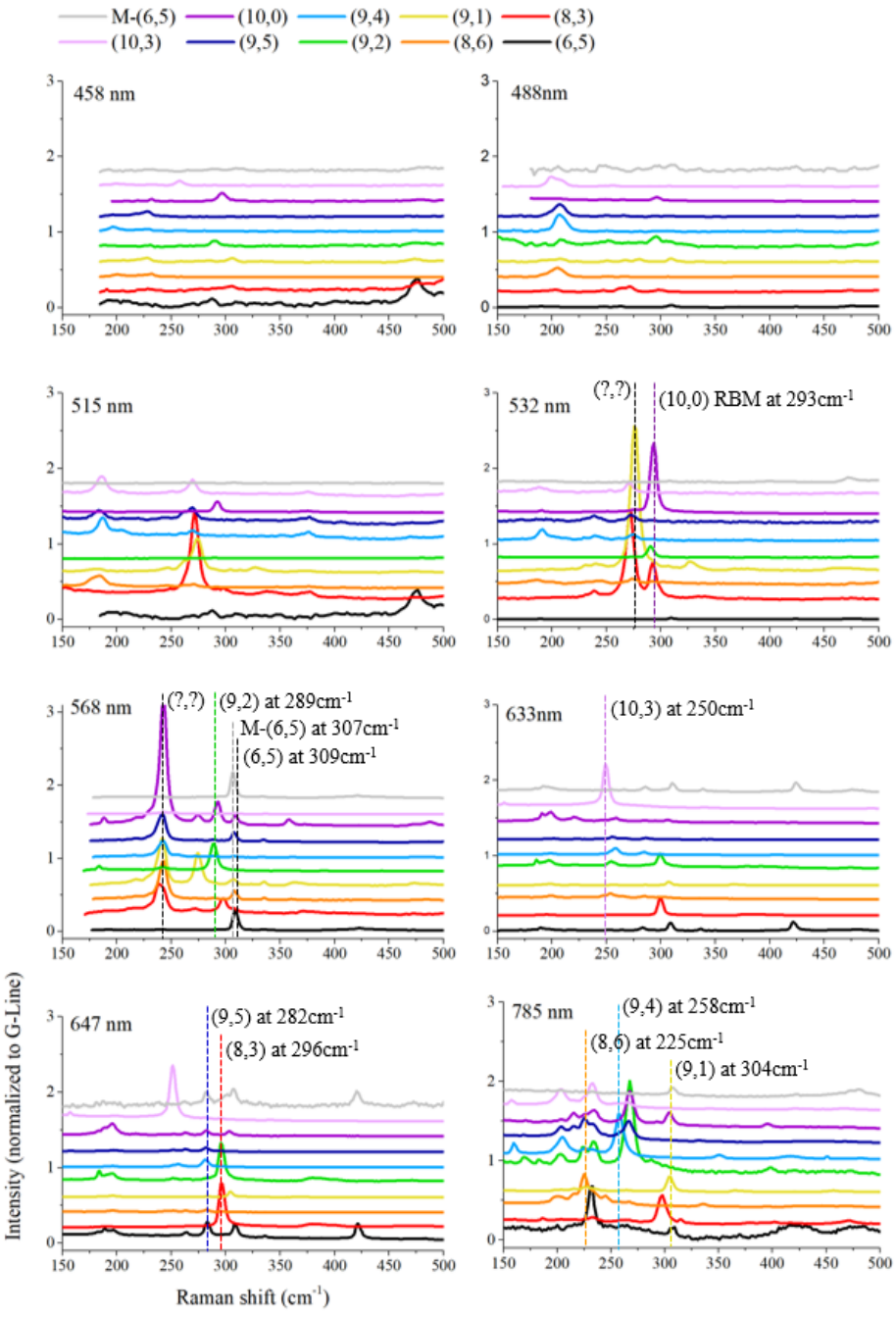

Figure 19: The Raman results from the LabRam in the RBM range from 150 to $500cm^{-1}$. Moreover, the results from the infrared $785nm$ WiTec are presented in the bottom right plot. The data is normalized to the G-line. The modes associated with the sample chiralities are denoted with a vertical dashed line. Two further striking RBM at $242cm^{-1}$ and $275cm^{-1}$ arise that stem from other nanotube types as discussed in section 4.2.

Besides the observation on mode frequency, we have the possibility to compare the RBM intensities with eachother. The intensities of (n,m) associated dominant RBM given in percent of G-line for the set of probes is summarized in table 6. The relative intensity is obtained as the maximum value of the RBM in the G line normalized spectra with subtraction of the background. In general, it is more precise to perform a Lorentzian peak fit when multiple features superimpose eachother and integrate the fitted curve. The chosen method is suited in this case, because the peaks are well separated and the relative maxima are sufficiently precise to estimate the enrichment. The values displayed in this manner contain two-fold information. Firstly, each row displays the identified nanotube types that are present and their intensity relative to the G line of this specimen. Only dominant breathing modes related to one of the ten structures are considered. It is evident that at least two more nanotube structures are coexisting, but they can be neglected for the depiction of enrichment between the set of ten types. Secondly, each column displays the RBM intensity corresponding to the enriched structure in the *different* specimen. To point out the findings in a more intuitive way figure 20 includes a stacked bar diagram with the relative RBM composition in each sample. The defined RBM values are normalized such that the sum of the ten modes equals 100%. The latter figure 21 shows the relative RBM intensity in the various specimen. The resulting relative RBM maxima are quantifying the selection process and express the enrichment.

Table 6: Every (n,m) structure of our sub-set has an associated dominant RBM. Each of them represent one column of the table. The first one represents the (6,5) tubes regardless the handedness. The second one represents the (8,3), the third one the (8,6) and so on until the RBM at 250 wavenumbers that represents the (10,3) tubes. The rows are defined by the ten samples, named after the enriched (n,m) structure. The elements of the table are the height of the RBM, given in relation to the G peak. Focusing on one specific row, e.g. sample (6,5), one sees which other breathing modes are present. Thereby, only breathing modes associated with one of the enriched chiralities are taken into account. Focusing on one column one sees in which specimen the different modes arise.

ν_{RBM} (cm^{-1})	309	296	225	304	289	258	282	293	250
Laser (nm)	568	647	785	785	568	785	647	532	647
Sample	RBM/G line								
(6,5)	0.285	0	0	0.128	0	0.042	0.185	0	0
(8,3)	0.084	0.606	0	0	0	0	0	0.454	0
(8,6)	0.143	0	0.388	0	0	0	0.041	0	0.052
(9,1)	0.010	0	0	0.206	0	0	0	0	0
(9,2)	0	0.502	0.213	0	0.377	0	0	0.160	0.062
(9,4)	0	0	0.073	0	0	0.552	0.093	0	0.072
(9,5)	0.147	0	0.236	0	0	0.042	0.062	0	0
(10,0)	0.124	0	0.078	0.171	0.121	0	0.062	0.913	0
(10,3)	0	0	0	0	0	0.007	0	0	0.566
M-(6,5)	0.355	0.098	0	0.103	0	0	0.155	0	0

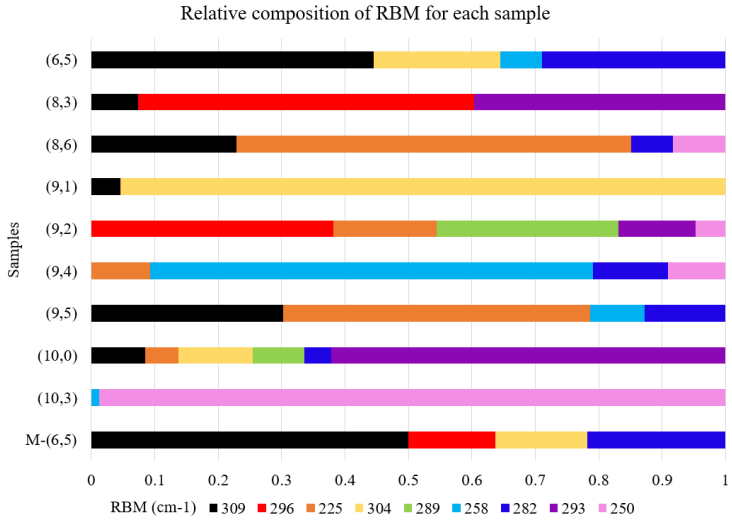

Figure 20: The relative composition of the defined RBM shown in a stacked bar diagram. The values are normalized to yield a total sum of 1 for the composition in each specimen.

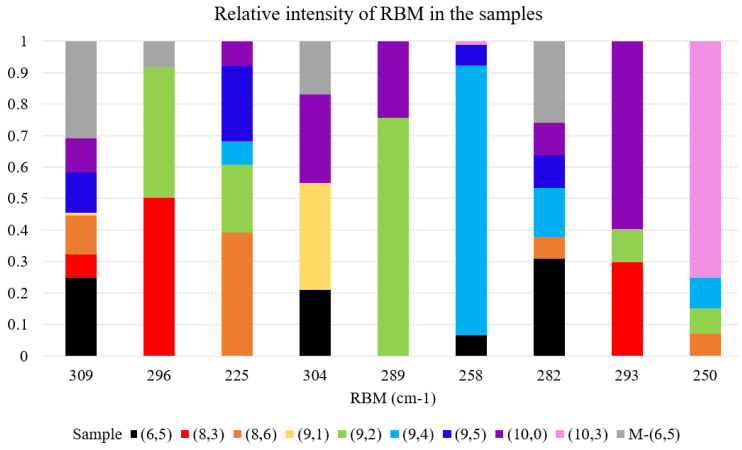

Figure 21: The relative intensity of each defined RBM in the various samples, shown in a stacked bar diagram. The relative values provide insight about the content of one specific chirality, or an associated RBM, in the various specimen. It is a measure for the enrichment when the RBM bar is intensified for the related enriched sample. In other words, a perfectly sorted set of samples will lead to "single-colour" bars in the diagram. For example the $258cm^{-1}$ RBM arises most intense and almost solely in sample (9,4).

The multi-column gel-chromatography process yields in a clearly dominant RBM in the enriched probes. Specimen enriched with nanotubes of (6,5), M-(6,5), (8,3), (9,2) and (10,0) type can be efficiently enhanced by one of the present laser excitations. Although, the gas lines are varyingly appropriate for the transition energies, some qualitative information is gained. From the top figure 20 information on the selection process is visible. The majority of the samples show 50% or more of the enriched (n,m), i.e. the dominant RBM related to it, in the relative composition. Sample (9,1) and (10,3) have almost solely the defined dominant breathing mode and only a minor peak at $309cm^{-1}$ or $258cm^{-1}$ respectively. The pair of plus- and minus (6,5) sorted samples shows a similar relative composition with around 50% of the (6,5) related RBM. An exception is the (9,5) structure, because no enrichment of the $282cm^{-1}$ RBM can be observed using this method. The structures E_{22} transition energy is given by $1.845eV$ (672nm) and hence the dominant resonance frequency $\nu_{\mathrm{RBM}} = 282cm^{-1}$ was assessed from the spectrum of $647nm$. Even though the Raman is powerful to sense SWCNT related phonons, the resonance was too far to efficiently sense the (9,5) breathing mode. There are two main assumptions that must be fulfilled to properly compare the RBM maxima. Firstly, the allocation of the dominant RBM is only possible if the structure is close to resonance for one of the lasers. This is not given for the (9,5) structure and the enhancement is insufficient to obtain related mode intensities. The defined dominant mode yields only a relative intensity of 12%, shown as the dark blue bar in the diagram. To unmistakably identify the right RBM a further laser line is necessary. Secondly, the normalization of absolute intensities to the G mode is applicable only when the contributing carbon material is proportional to the present semiconducting SWCNT. This is not the case if one of the specimen contains a fraction of other carbon material. In fact, the presence of at least two additional types of nanotubes with diameters of 0.97nm and 0.87nm is concluded from striking breathing modes at $242cm^{-1}$ (resonant at 568nm) and $270cm^{-1}$ (resonant at 532nm).

From the relative mode intensity grouped by the various specimen in which it arises, depicted as the bar diagram in figure 21, the enrichment is estimated. A fictional bar diagram for ideal enrichment, where only one SWCNT chirality remains, is shown in the appendix 27 for illustration purposes. This means that the (6,5) and M-(6,5) specimen contain 20% and 30% of all nanotubes related to the $309cm^{-1}$ breathing mode respectively. The (8,3) sample is responsible for 50% of the total RBM signal at $296cm^{-1}$. The species with the highest enrichment, hence closest to a "single-coloured" bar, are (10,3), (9,4) and (9,2). The relative RBM yields 75% or more in the enriched sample, compared to a very minor contribution in other samples. Very interesting is the distribution of RBM originating from the (9,5) sample, shown in dark blue. The specimen includes breathing modes at $309cm^{-1}$, $225cm^{-1}$, $258cm^{-1}$ and $282cm^{-1}$. Nevertheless, the breathing mode at 282 should be excluded from the analysis due to the before explained reasons. relative rates adding up to 100% between the specimen are newly calculated and result in the figure 22.

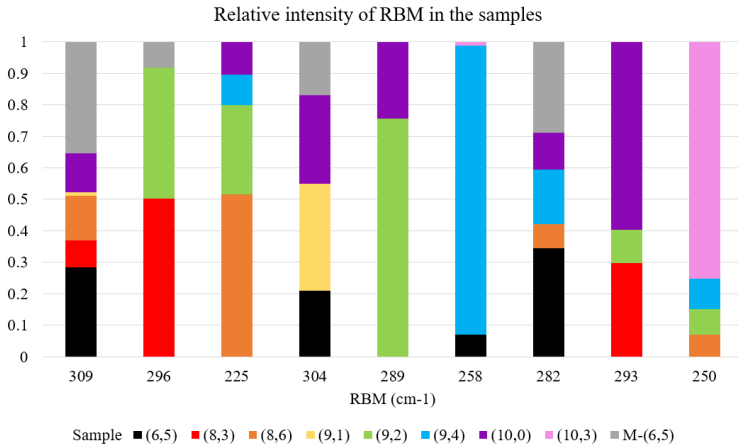

Figure 22: The relative intensity of each defined RBM in the sub-set of samples, shown in a stacked bar diagram. The relative values can be investigated for any series of samples. It is a measure for the contribution to a RBM from different mixtures.

The normalization is subject to the considered breathing modes. For specimen after successful selective processing the expected RBM is known. To detect the full composition of chiralities however, various lasers are necessary to probe possibly resonant other structures. The RBM profiling represents the full chirality composition if resonant lasers for all different chiralities are available. Hence, for a higher number of excitations the findings augment to display the whole picture. To sum up, the method of RBM profiling improves to represent the chirality composition with an increasing number of laser energies or with better enriched specimen.

4.5 Resonance profiles of left and right-handed enantiomers

The characteristics of a certain REP can indicate a distribution of nanotubes in a cluster. When the resonance profile is unusually broad, it suggests that a series of various nanotubes emerge in resonance. The dye molecule Rhodamin 6G has a relatively narrow spectral exitance, but its maximum is close to the incoming resonance of the (6,5) SWCNT. The resonance profile of this sample as well as the lefthanded counterpart, is measured in steps of 2nm with the triple monochromator Raman setup. The dye emission provides a operation window between 564 and 578nm. This equals an energy window of $\Delta E_{exc} = 54meV$. The information sheet on available dyes applicable for the YAG pump laser and their emission limits is provided by the manufacturer and added in the appendix (A.6). Figure 23 illustrates a plot of the measured spectra for the series of excitations on the y-axis. The Intensity in counts per second on the z-axis in dependence of Raman shift in wavenumbers and excitation in eV. The closer the laser operates to the resonance, the higher the RBM signal. The interpolation

of the data points is background-subtracted and integrated. The resulting RBM area per watts is compared with each other. The similar process is repeated for the G line and both results are shown in figure 24. A complete table summarizing the excitation energy, the power, the mode intensity, the integrated value and the integrated devided by the power is found in the appendix table A.5.
The power stability of the dye laser is low and it operates in a pulsed manner with pulse lengths in the magnitude of nanoseconds. Therefore, it is decided to not exceed $0.5mW$ on average on the sample to ensure a constant operation. Still, it was experienced that the output power dropped drastically in some cases for a not clarified reason. The fact that it was not captured constantly during the measurements is a vacancy in data quality. For this reason the results are shown before division through the output power as well. Thereby, the maximum G intensity for the (6,5) structure in the depicted range clearly is at 570nm incident laser wavelength. However, the resonance profile traverses not the whole decline in intensity for shorter wavelengths. The sensitivity of the available dye Rhodamin 6G diminishes rapidly at the edge of the range. To span the whole profile, a necessary next step would be to change the dye system to Coumarin 153, which emitts between 520nm and 570nm with a maximum efficiency of 17%. This prospective is even clearer for the M-(6,5) species. The Raman response intensity of M-(6,5) was approximately 30% of the intensity achieved with (6,5), which is most probably based on different concentrations. Looking at the sample description one can definitely discern a difference in the colour. The resonance of this nanotube type lacks a convincing maximum and is without a clear trend for both analysed RBM and G vibrational modes. After normalization with the measured power the trend of decreasing G line intensity for higher excitation energy is evened out, because the output lasing power is low for operation near the edges of the dye emission spectrum. Altogether, a full resonance profile spanning an excitation range of at least $200meV$ instead of only $54meV$ would be of great interest. To conclude on the actual resonance and hence transition energy from the current profile is not possible.

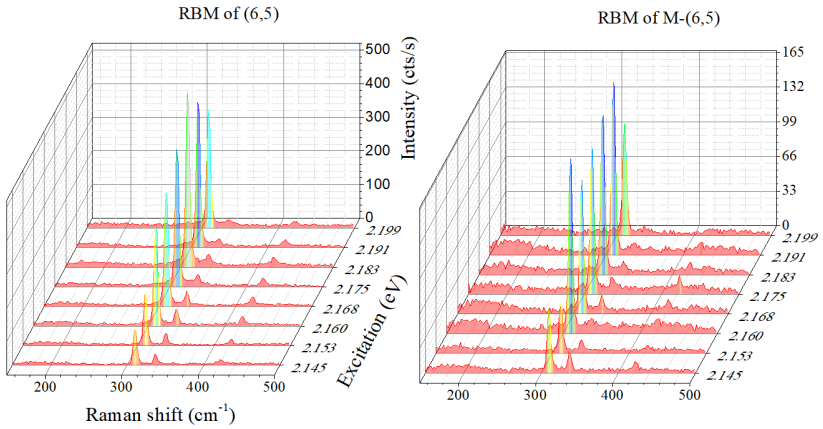

Figure 23: The RBM resonance profile for the (6,5) sample and its left-handed associate measured in steps of $\Delta\lambda_{exc} = 2nm$ over the range of $564nm$ (2.199eV) to $578nm$ (2.145eV). The intensity is shown in counts per second, attention to the lower counting rate with a maximum of 167 for M-(6,5) compared to a maximum of 520 for (6,5).

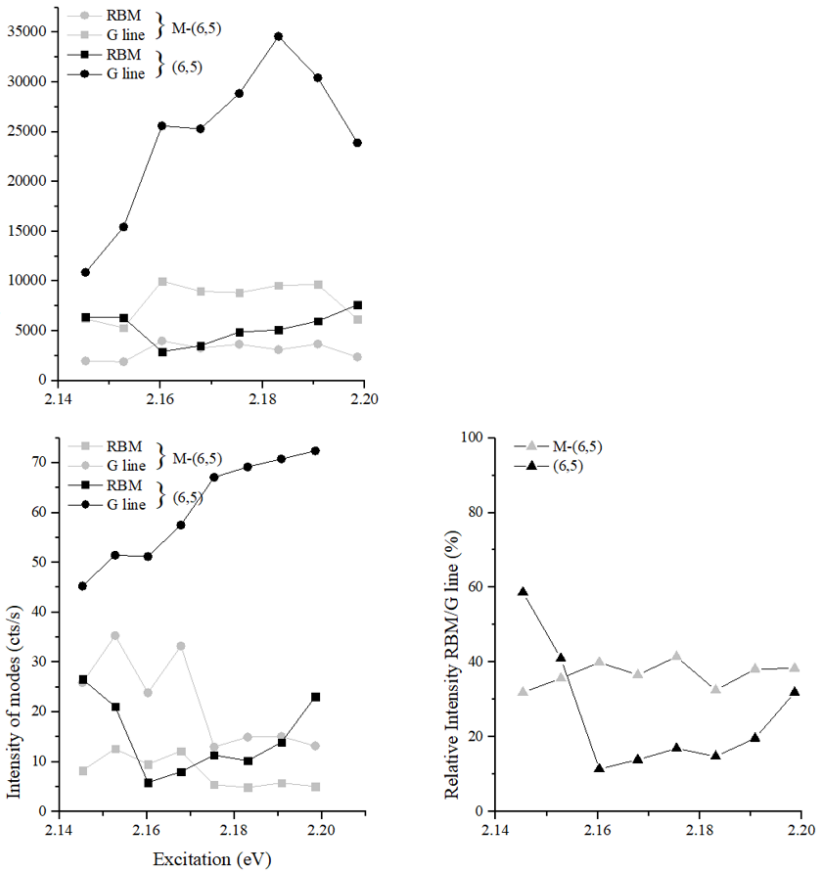

Figure 24: The signal for the RBM (squared symbol) is integrated between 100 and $500cm^{-1}$ and for the G line (circular symbol) from 1400 to $1700cm^{-1}$. The plot in the top illustrates the resonance trend as obtained without normalization to the power on sample for comparison. The intensity is shown in counts per second without normalization (arbitrary units). Below there is the similar integrated intensity divided by the output power as measured with the photodiode sensor. On the right hand side plotted is the relative intensity between both vibrational modes in percent (triangular symbol). Again the measurements are done in steps of $\Delta\lambda_{exc} = 2nm$ over the range of $564nm$ (2.199eV) to $578nm$ (2.145eV). The black curves are dedicated to the (6,5) structure and the grey one to the mirrored structure in consistency with the numerous plots.

5 Conclusion

Ten single-chirality SWCNT samples are investigated by Raman spectroscopy techniques to elucidate their properties after post-synthesis sorting. The electronic band gap of semiconducting carbon nanotubes is inversely proportional to their diameter. Cutting lines nestling on the energy surface of graphene are dependent on the chirality. In this manner the quantum confinement condition defines the sharp maxima in the density of states, referred to as van Hove singularities. The unique properties related to the individual carbon nanotubes, promise high potential future applications, especially for (opto-) electronic devices and nanotechnology [3]. However, challenges arise in the structure selective synthesis and sorting, what highlights the importance of characterization techniques. The usual Raman scattering signal is weak, but the scattering efficiency is enhanced when the excitation energy matches a transition energy between optically allowed electronic transitions in the material. The tables that contain the G line area per mW (A.3) show that the signal differs by a factor of 50 or 80 between the operation of different gas lines. This sensitivity makes it possible to compare the phonon frequencies related to the circumference of SWCNT. The reports on the diameter and transition energies of the investigated species from an comprehensive empirical Kataura plot are presented [25]. The experimentally obtained breathing mode frequencies are used to conduct own calculations of the diameter. They match the predictions with an average deviation as low as 4%. The small diameter nanotubes are clearly associated with the enriched (n,m) labelling on their containers. The used A parameter, which stems from the velocity of the LO mode, is proposed in literature [36,37,43]. The inspection of the distribution of nanotubes on the droplets surface is concluded from relative contrast in the camera mode of the specific system. The findings from the Fourier transform Raman spectroscopy also show that the sample distributes on the droplet with different thickness. The structural quality of nanotubes is quantified by the in-sheet breathing mode of carbon hexagons, referred to as D line. The D/G ratio is high for the (10,0) specimen with striking 32%, which indicates defects in the material. All other samples depict a less intense D line with maximal 8% relative intensity compared to the G line.

Two sample preparation methods are chosen with individual advantages and disadvantages. The fully dried droplets (dropcast) on Si substrate are easy to handle and to focus under the optical microscope, display a known reference peak at $521cm^{-1}$ and fit in numerous sample holders regardless the orientation. However, the FT Raman indicates an inhomogeneous distribution of SWCNT. The periodic background is a consequence of inhomogenous layer thickness, in particular interference from spots with different path length. It is supposed that the samples with a lower density in sample distribution, have more reflection from the underlying Si and therefore a higher laser-line. This assumption is consistent with the statement of layer interference, as those are the samples with the most prominent periodic background. The capillaries filled with an amount of approximately $2\mu l$ of aqueous solution containing the single structure enhanced

SWCNT have the advantage of naturally averaging the signal as one probes a liquid. For the comparison of either environmental effects on the nanoscale, Raman shift sensitive interactions are analysed. In particular bundles of multiple tubes will display van der Waals interactions, which can influence specific vibrational modes. Such a collective vibration features a RBM frequency different from individual nanotubes, which is analysed by peak position for solid state versus liquid. The study elucidated that no significant differences larger than the spectral resolution of the system arise during the drying process. Therefore, I propose the usage of dropcasts when operating with a continuous excitation source. If a pulsed laser is used, the capillaries are the better option, as they are more resistant to burning damage.

The Raman spectra of the investigated samples provided by *Kataura et al.* show multiple RBM in resonance with different laser excitation. This attests the presence of various carbon nanotubes with transition energies over the visible range. At least two nanotube chiralities are present, which are not covered in our sub-set of the ten enriched species. This is demonstrated by the occurrance of two unidentified RBM, which could be assigned to the corresponding chirality by REP in a prospective study. However, the gel interaction during the process of multi-column gel-chromatography, clearly results in selective enrichment. The difference in colour characteristics is visible with the bare eye, ranging from violet to dark green. The enrichment is validated quantitatively in figure 21 and yields a clearly dominant RBM in the enriched probes. More than 50% of the relative mode intensities stem from the dominant RBM in most of the specimen. The most prominent enrichment is achieved for (9,1) and (10,3) with over 95% relative RBM related to the enriched nanotubes. However, no enrichment of the (9,5) sample could be elucidated by the chosen method. The reason is that the structure does not display a resonant RBM with sufficient intensity for the available lasers. The dominant RBM that is supposed for the (9,5) chirality is responsible for only 12% of the total modes defined. It even arises 3 times and 2.5 times higher in the (6,5) and M-(6,5) specimen than in the (9,5) sample respectively. Most probably, it is not associated with an (n,m) type of our set. The set of mixtures or specimen contributing to a particular RBM can be expanded or scaled-down as required. This is the main strength of the chosen method and presentation. The RBM profiling gets more precise in determining the chirality distribution the more excitations are available. To effectively investigate the whole set additional laser lines would be necessary as summarized in table 4.4. The thesis elucidates the stage of sorting by multi-column gel-chromatography is still apart from the desired single-chirality, but the post-synthesis processing leads to a significant improvement.

References

[1] K. Kim, J. Y. Choi, T. Kim, S. H. Cho, and H. J. Chung, "A role for graphene in silicon-based semiconductor devices," *Nature*, vol. 479, no. 7373, pp. 338–344, 2011.

[2] G. J. Brady, A. J. Way, N. S. Safron, H. T. Evensen, P. Gopalan, and M. S. Arnold, "Quasi-ballistic carbon nanotube array transistors with current density exceeding Si and GaAs," *Science Advances*, vol. 2, no. 9, pp. 1–10, 2016.

[3] I. A. Kinloch, J. Suhr, J. Lou, R. J. Young, and P. M. Ajayan, "Composites with carbon nanotubes and graphene: An outlook," *Science*, vol. 362, no. 6414, pp. 547–553, 2018.

[4] S. Iijima, "Helical microtubules of graphitic carbon," *Nature*, vol. 354, pp. 56–58, 1991.

[5] J. W. Mintmire, B. I. Dunlap, and C. T. White, "Are fullerene tubules metallic?," *Physical Review Letters*, vol. 68, no. 5, pp. 631–634, 1992.

[6] M. Reibold, P. Paufler, and A. e. a. Levin, "Carbon nanotubes in an ancient Damascus sabre," *Nature*, vol. 444, 2006.

[7] L. Yu, C. Shearer, and J. Shapter, "Recent Development of Carbon Nanotube Transparent Conductive Films," *Chemical Reviews*, vol. 116, no. 22, pp. 13413–13453, 2016.

[8] M. J. Shea and M. S. Arnold, "1% Solar Cells Derived From Ultrathin Carbon Nanotube Photoabsorbing Films," *Applied Physics Letters*, vol. 102, no. 24, 2013.

[9] Y. Miyauchi, M. Iwamura, S. Mouri, T. Kawazoe, M. Ohtsu, and K. Matsuda, "Brightening of excitons in carbon nanotubes on dimensionality modification," *Nature Photonics*, vol. 7, no. 9, pp. 715–719, 2013.

[10] R. Martel, T. Schmidt, and H. e. a. Shea, "Single- and multi-wall carbon nanotube field- effect transistors," *Applied Physics Letters*, vol. 73, no. APL classic papers, pp. 24–27, 1998.

[11] H. Liu, T. Tanaka, and H. Kataura, "Optical isomer separation of single-chirality carbon nanotubes using gel column chromatography," *Nano Letters*, vol. 14, no. 11, pp. 6237–6243, 2014.

[12] D. Janas, "Towards monochiral carbon nanotubes: A review of progress in the sorting of single-walled carbon nanotubes," *Materials Chemistry Frontiers*, vol. 2, no. 1, pp. 36–63, 2018.

[13] S. K. Doorn, D. A. Heller, P. W. Barone, M. L. Usrey, and M. S. Strano, "Resonant Raman excitation profiles of individually dispersed single walled carbon nanotubes in solution," *Applied Physics A: Materials Science and Processing*, vol. 78, no. 8, pp. 1147–1155, 2004.

[14] H. Liu, D. Nishide, T. Tanaka, and H. Kataura, "Large-scale single-chirality separation of single-wall carbon nanotubes by simple gel chromatography," *Nature Communications*, vol. 2, no. 1, 2011.

[15] A. Jorio, R. Saito, G. Dresselhaus, and M. S. Dresselhaus, *Raman Spectroscopy in Graphene Related Systems*. 2011.

[16] X. Zhao, Y. Liu, S. Inoue, T. Suzuki, R. O. Jones, and Y. Ando, "Smallest carbon nanotube is 3 Å in diameter," *Physical Review Letters*, vol. 92, no. 12, pp. 12–14, 2004.

[17] R. Iii, C. Catalyzed, P. An, O.-s. S. Pyrene, J. Hu, D. Zhang, and F. W. Harris, "Growth of Half-Meter Long Carbon Nanotubes Based on Schulz-Flory Distribution," *ACS Nano*, no. 550mm long CNT, pp. 1–13, 2013.

[18] A. Galano, "Carbon nanotubes : promising agents against free radicals," *Nanoscale*, vol. Advance Ar, pp. 373–380, 2010.

[19] G. Ao, J. K. Streit, J. A. Fagan, and M. Zheng, "Differentiating Left- and Right-Handed Carbon Nanotubes by DNA," *Journal of the American Chemical Society*, vol. 138, pp. 16677–16685, 12 2016.

[20] N. Komatsu, "Stereochemistry of Carbon Nanotubes," *Jps. J. Appl. Physics*, vol. 49, 2010.

[21] J. C. Charlier, X. Blase, and S. Roche, "Electronic and transport properties of nanotubes," *Reviews of Modern Physics*, vol. 79, no. 2, pp. 677–732, 2007.

[22] S. Reich, J. Maultzsch, C. Thomsen, and P. Ordejón, "Tight-binding description of graphene," *Physical Review B - Condensed Matter and Materials Physics*, vol. 66, no. 3, pp. 354121–354125, 2002.

[23] M. S. Dresselhaus, G. Dresselhaus, R. Saito, and A. Jorio, "Raman spectroscopy of carbon nanotubes," *Physics Reports*, vol. 409, no. 2, pp. 47–99, 2005.

[24] J. G. Duque, H. Telg, H. Chen, A. K. Swan, A. P. Shreve, X. Tu, M. Zheng, and S. K. Doorn, "Quantum interference between the third and fourth exciton states in semiconducting carbon nanotubes using resonance Raman spectroscopy," *Physical Review Letters*, vol. 108, no. 11, pp. 1–5, 2012.

[25] R. B. Weisman and S. M. Bachilo, "Dependence of optical transition energies on structure for single-walled carbon nanotubes in aqueous suspension: An empirical Kataura plot," *Nano Letters*, vol. 3, no. 9, pp. 1235–1238, 2003.

[26] A. Jorio, M. A. Pimenta, C. Fantini, M. Souza, A. G. Filho, G. G. Samsonidze, G. Dresselhaus, M. S. Dresselhaus, and R. Saito, "Advances in single nanotube spectroscopy: Raman spectra from cross-polarized light and chirality dependence of Raman frequencies," *Carbon*, vol. 42, no. 5-6, pp. 1067–1069, 2004.

[27] H. Kuzmany, *Solid-State Spectroscopy.* Springer, 2009.

[28] T. Schmid and P. Dariz, "Raman Microspectroscopic Imaging of Binder Remnants in Historical Mortars Reveals Processing Conditions," *Heritage*, vol. 2, no. 2, pp. 1662–1683, 2019.

[29] K. C. W. B. Ferraro, J. R.; Nakamoto, *Introductory Raman Spectroscopy.* Academic Press,An imprint of Elsevier Science, second ed., 2003.

[30] F. Simon, R. Pfeiffer, and H. Kuzmany, "Universal temperature dependence of optical excitation life-time and band-gap in chirality assigned semiconducting single-wall carbon nanotubes,"

[31] H. Kuzmany, W. Plank, M. Hulman, C. Kramberger, A. Grüneis, T. Pichler, H. Peterlik, H. Kataura, and Y. Achiba, "Determination of SWCNT diameters from the Raman response of the radial breathing mode," *European Physical Journal B*, vol. 22, no. 3, pp. 307–320, 2001.

[32] E. H. Hároz, J. G. Duque, E. B. Barros, H. Telg, J. R. Simpson, A. R. Hight Walker, C. Y. Khripin, J. A. Fagan, X. Tu, M. Zheng, J. Kono, and S. K. Doorn, "Asymmetric excitation profiles in the resonance Raman response of armchair carbon nanotubes," *Physical Review B - Condensed Matter and Materials Physics*, vol. 91, 5 2015.

[33] P. Larkin, "Introduction," *Infrared and Raman Spectroscopy*, pp. 1–5, 2011.

[34] A. I. Abd El-Mageed, M. Handayani, Z. Chen, T. Inose, and T. Ogawa, "Assignment of the Absolute-Handedness Chirality of Single-Walled Carbon Nanotubes Using Organic Molecule Supramolecular Structures," *Chemistry - A European Journal*, vol. 25, no. 8, pp. 1941–1948, 2019.

[35] V. N. Popov, V. E. V. Doren, and M. Balkanski, "Lattice dynamics of single-walled carbon nanotubes," vol. 59, no. 13, pp. 8355–8358, 2020.

[36] G. D. Mahan, "Oscillations of a thin hollow cylinder: Carbon nanotubes," *Physical Review B - Condensed Matter and Materials Physics*, vol. 65, no. 23, pp. 1–7, 2002.

[37] M. J. Longhurst and N. Quirke, "The environmental effect on the radial breathing mode of carbon nanotubes in water," *Journal of Chemical Physics*, vol. 124, no. 23, 2006.

[38] A. Jorio, M. A. Pimenta, A. G. Souza Filho, R. Saito, G. Dresselhaus, and M. S. Dresselhaus, "Characterizing carbon nanotube samples with resonance Raman scattering," tech. rep., 2003.

[39] L. G. Moura, M. V. Moutinho, P. Venezuela, F. Mauri, A. Righi, M. S. Strano, C. Fantini, and M. A. Pimenta, "The double-resonance Raman spectra in single-chirality (n, m) carbon nanotubes," *Carbon*, vol. 117, pp. 41–45, 2017.

[40] J. Maultzsch, H. Telg, S. Reich, and C. Thomsen, "Radial breathing mode of single-walled carbon nanotubes: Optical transition energies and chiral-index assignment," *Physical Review B - Condensed Matter and Materials Physics*, vol. 72, no. 20, pp. 1–16, 2005.

[41] K. Hashimoto and T. Ideguchi, "Phase-controlled Fourier-transform spectroscopy," *Nature Communications*, vol. 9, no. 1, pp. 1–7, 2018.

[42] G. E. Walrafen, "Raman spectrum of water: Transverse and longitudinal acoustic modes below 300 cm-1 and optic modes above 3OO cm-1," *Journal of Physical Chemistry*, vol. 94, no. 6, pp. 2237–2239, 1990.

[43] A. Jorio, M. A. Pimenta, A. G. Souza Filho, R. Saito, G. Dresselhaus, and M. S. Dresselhaus, "Characterizing carbon nanotube samples with resonance Raman scattering," tech. rep., 2003.

A Appendix

A.1 Danksagung/Acknowledgement

An dieser Stelle möchte ich mich zuerst bei meinem Betreuer Professor Thomas Pichler bedanken, für die Möglichkeit eine spannende Masterarbeit im Rahmen der Forschungsgruppe *Electronic Properties of Materials* zu erstellen. Den interessierten Umgang miteinander und den unkomplizierten Zugang zu benötigten Gerätschaften schätze ich sehr. Auch während der Home-Office Phase aufgrund der Pandemie 2020 fühlte ich mich gut betreut und so wurden Diskussionen einfach in die Cloud verlegt.
Ein großes Danke richte ich auch an Dr. Christian Kramberger, für den spannenden Austausch in dieser letzten Phase meines Studiums. Ich schätze es sehr, dass ich stets mit meinen Anregungen und Fragen einen Ansprechpartner hatte. Ich habe viel gelernt und hatte dennoch große Freiheit im Labor und bei der Anfertigung der Arbeit, Danke.
A special thank you to Valeria Milotti, who always had an open ear, an advice and a joke during the laboratory time. You are truly a role model to students in the field. My appreciation also to Yifan Zhang, for the expert opinion and helpful talks regarding the dye laser.

A.2 Raman spectra without zoom ins

Figure 25: The full range Raman spectra without axis breaks to focus on RBM, G line and 2D line for the dropcasts. The D line near $1300cm^{-1}$ depicts a relative intensity of up to 27% compared to the G line. It originates from disordered structures, i.e. defects in sp^2 hybridized carbon structures. As discussed from the FT spectra in figure 16. Further minor peaks occur near $1000cm^{-1}$, which are not resulting from an identified vibrational mode of SWCNT. The prominent feature at a Raman shift of $521cm^{-1}$ is coming from the Si background.

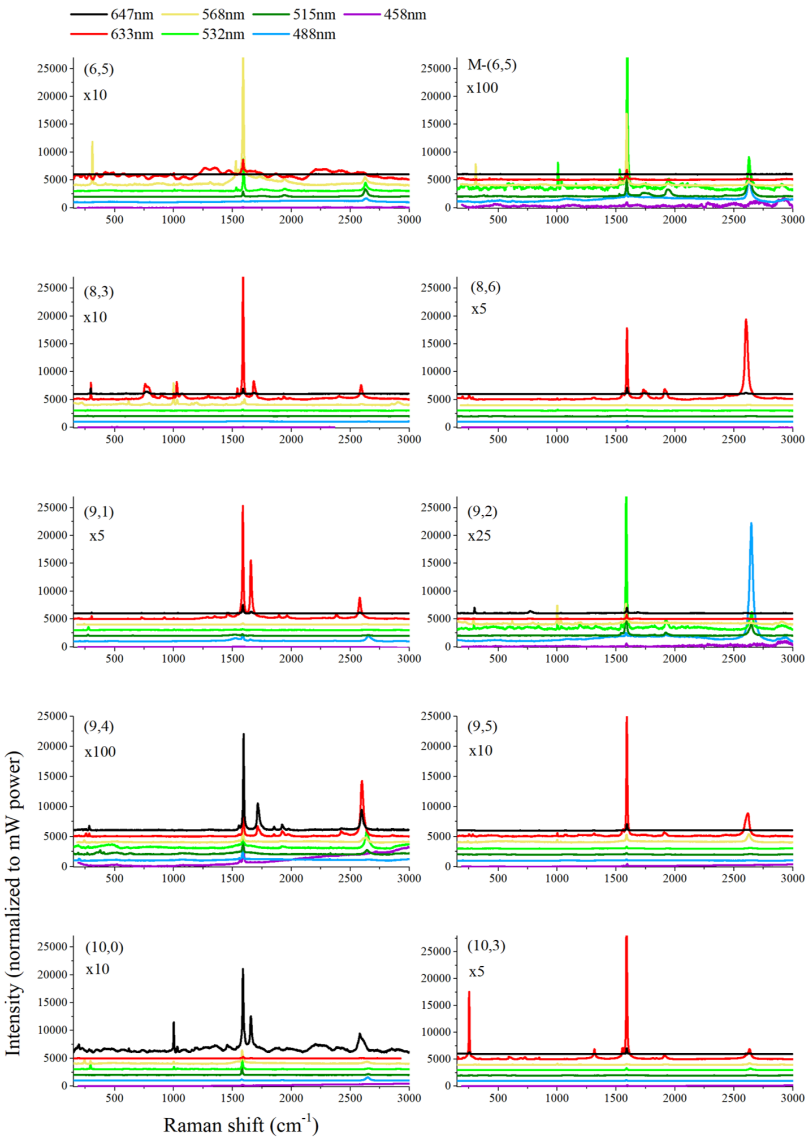

Figure 26: The plots gathered similarily to above, but with the data normalized by the output power, for the liquid samples. The intensity is given in arbitrary units, but the axis section is equal for all samples from 0 to 25000. The multiplication factor for the data is given below the (n,m) type. This makes the comparison much more convenient. The glass supports instead of Si do not result in a characteristic feature, which was quite useful in terms of having a reference peak.

A.3 Tables of absolute intensity (G Area/W)

Table 7: The area under the G line intensity curve between 1400 and 1700cm^{-1} devided by the mW power on sample. The table is put here in addition, because the normalization chosen in figure 14 has the disadvantage of losing the absolute itensity maxima.

Excitation (nm)	458	488	515	532	568	633	647
Power (mW)	0.4	1	0.5	0.4	1	0.7	1
(n,m)	Area/W						
(6,5)	4.85	139.76	40.34	137.14	205.73	223.163	15.88
(8,3)	12.27	156.46	8.33	56.25	15.07	217.45	68.84
(8,6)	305.12	40.59	34.29	23.31	20.65	23.02	19.81
(9,1)	23.71	76.01	154.97	114.87	42.86	273.11	40.87
(9,2)	8.31	10.22	76.69	25.17	88.57	26.85	9.76
(9,4)	27.96	30.44	42.62	66.19	84.01	283.89	147.19
(9,5)	22.25	25.51	14.70	12.46	28.30	30.64	36.93
(10,0)	14.29	65.49	26.98	183.81	58.69	29.67	16.61
(10,3)	10.49	18.00	17.74	8.61	101.52	643.89	37.23
M-(6,5)	6.81	3.87	199.28	26.60	80.88	22.52	1.69

Table 8: Similar table for the sealed capillaries. The G lines absolute intensity is approximately one third compared to the intensity from dropcasts.

Excitation (nm)	458	488	515	532	568	633	647
Power (mW)	0.4	1	0.5	0.4	1	0.7	1
(n,m)	Area/W						
(6,5)	4.85	139.76	40.34	137.14	205.73	223.163	15.88
(8,3)	12.27	156.46	8.33	56.25	15.07	217.45	68.84
(8,6)	305.12	40.59	34.29	23.31	20.65	23.02	19.81
(9,1)	23.71	76.01	154.97	114.87	42.86	273.11	40.87
(9,2)	8.31	10.22	76.69	25.17	88.57	26.85	9.76
(9,4)	27.96	30.44	42.62	66.19	84.01	283.89	147.19
(9,5)	22.25	25.51	14.70	12.46	28.30	30.64	36.93
(10,0)	14.29	65.49	26.98	183.81	58.69	29.67	16.61
(10,3)	10.49	18.00	17.74	8.61	101.52	643.89	37.23
M-(6,5)	6.81	3.87	199.28	26.60	80.88	22.52	1.69

A.4 Fictional relative RBM intensity after ideal enrichment

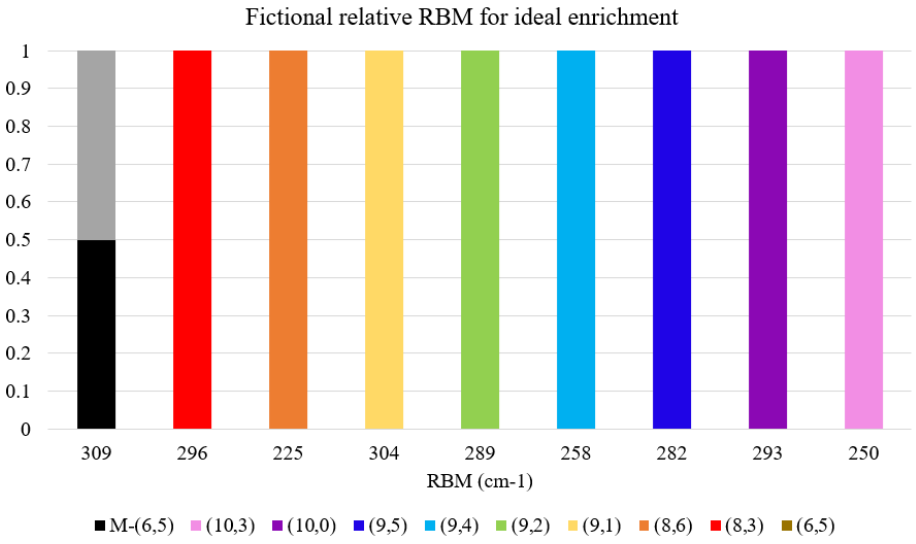

Figure 27: After an optimal selection process the chiralities are sorted and each breathing mode arises in only one enriched sample. The figure is added for illustration purposes and can be compared to the actual results in figure 21.

A.5 Table of RBM and G line resonance profile

Table 9: Summary of the RBM and G line signal for the series of excitations with the tunable laser system. The columns depict the peak maximum (Max), the integrated signal (Area) and the area per watt output power as measured with the photodiode (Area/W). The integration limits are from 100 to 500 wavenumbers and from 1400 to 1700 wavenumbers for the RBM and G line respectively.

(6,5)								
λ_{exc} (nm)	E_{exc} (eV)	RBM Max (a.u.)	Gline Max	Power (mW)	RBM Area	G line Area	RBM Area/W	G line Area/W
564.000	2.199	351.380	1021.070	0.330	7613.690	23892.200	23.072	72.401
566.000	2.191	433.092	1289.370	0.430	5973.980	30430.000	13.893	70.767
568.000	2.183	519.595	1648.360	0.500	5097.570	34598.500	10.195	69.197
570.000	2.175	409.056	1403.710	0.430	4872.870	28852.900	11.332	67.100
572.000	2.168	338.979	1284.330	0.440	3509.090	25307.000	7.975	57.516
574.000	2.160	293.804	1248.680	0.500	2915.250	25592.200	5.831	51.184
576.000	2.153	152.985	731.329	0.300	6322.640	15436.700	21.075	51.456
578.000	2.145	107.644	513.123	0.240	6377.660	10866.200	26.574	45.276
M-(6,5)								
564.000	2.199	106.960	271.700	0.470	2370.080	6186.300	5.043	13.162
566.000	2.191	164.853	420.229	0.640	3679.650	9651.110	5.749	15.080
568.000	2.183	151.951	440.251	0.640	3105.000	9562.300	4.852	14.941
570.000	2.175	139.013	392.461	0.680	3659.480	8832.870	5.382	12.990
572.000	2.168	128.055	365.300	0.270	3281.530	8971.590	12.154	33.228
574.000	2.160	166.910	420.093	0.420	3995.630	10005.600	9.513	23.823
576.000	2.153	52.577	188.629	0.150	1888.230	5297.800	12.588	35.319
578.000	2.145	61.158	264.344	0.240	1978.860	6207.760	8.245	25.866

Data for Dyes for Nd: YAG Laser Pumped Dye Lasers

Dye	Peak (nm)	Tuning Rang (nm)	Solvent	Concentr. (g/l)	Effic. (%)	Pump Wavelenght
PTP	340	333-348	CH	0,16	6	266
Butyl-PBD	365	355-389	CH	0,45	5	266
Exalite 376	376	369-381	DI	0,15	15	355
Exalite 384	384	377-388	DI	0,3	17	355
Exalite 389	389	378-395	DI	0,2	20	355
Exalite 398	398	391-404	DI	0,3	22	355
RDC 387**	387	390-396	DI	0,13	18	355
BiBuQ	390	380-410	EtOH/TO	1,4	4	355
Stilbene 3	425	414-445	EtOH	0,2	17	355
Coumarin 120	440	428-453	EtOH	0,2	15	355
Coumarin 47	455	440-468	Isopr.	0,21	14	355
Coumarin 47	460	446-478	EtOH	0,25	14	355
Coumxrin 102	471	450-485	Isopr.	0,53	14	355
Coumarin 102	481	460-495	EtOH	0,4	14	355
Coumarin 307	500	475-510	Isopr.	0,33	18	355
Coumarin 307	508	488-540	EtOH	0,4	18	355
Coumarin 152	518	490-540	Isopr.	0,3	15	355
Coumarin 152	525	510-565	EtOH	0,3	15	355
Coumarin 153	535	515-560	Isopr.	1,7	18	355
Coumarin 153	540	515-570	EtOH	2,5	18	355
Flouxscein 27	548	539-590	ME basic	0,8	30	532
Rhodamine 6G*	565	554-585	EtOH	0,14	30	532
Rhodamine B	580	590-605	EtOH	0,2	28	532
Sulforrhodamine B	587	580-620	EtOH	0,26	28	532
DCM	640	607-663	EtOH	0,35	30	532
DCM	660	620-687	DMSO	0,4	30	532
DCM/Pyridine 1		630-680	Isopr.	0,8/0,2	20	532
RDC 650		630-720	DMSO	0,1	14	532
Pyridine 1	698	665-725	EtOH	0,3	20	532
Pyridine 2	722	695-745	EtOH	0,26	22	532
Styryl 7	720	701-749	EtOH	0,12	18	532
Styryl 8	750	720-777	EtOH	0,15	9	532
Styryl 9	816	790-845	EtOH	0,14	11	532
LDS 867	866	830-910	EtOH	0,15	15	532
LDS 925	960	870-1040	EtOH	0,8-1,2	11	532

* Rhodamine B and Rhodamine 6G can be mixed. Thus the tuning ranges can be shifted.

** Extremly long lifetime